MNRAS **528,** 3198–3216 (2024) Advance Access publication 2023 December 20

# *In-situ* versus accreted Milky Way globular clusters: a new classification method and implications for cluster formation

Vasily Belokurov <sup>10</sup> and Andrey Kravtsov <sup>10</sup> 2,3,4★

- <sup>1</sup>Institute of Astronomy, Madingley Rd, Cambridge CB3 0HA, UK
- <sup>2</sup>Department of Astronomy and Astrophysics, The University of Chicago, Chicago, IL 60637, USA
- <sup>3</sup>Kavli Institute for Cosmological Physics, The University of Chicago, Chicago, IL 60637, USA

Accepted 2023 December 12. Received 2023 December 9; in original form 2023 September 28

#### **ABSTRACT**

We present a new scheme for the classification of the *in-situ* and accreted globular clusters (GCs). The scheme uses total energy E and z-component of the orbital angular momentum and is calibrated using the [Al/Fe] abundance ratio. We demonstrate that this classification results in two GC populations with distinct spatial, kinematic, and chemical abundance distributions. The *in-situ* GCs are distributed within the central 10 kpc of the Galaxy in a flattened configuration aligned with the Milky Way (MW) disc, while the accreted GCs have a wide distribution of distances and a spatial distribution close to spherical. *In-situ* and accreted GCs have different [Fe/H] distributions with the well-known bimodality present only in the metallicity distribution of the *in-situ* GCs. Furthermore, the accreted and *in-situ* GCs are well separated in the plane of [Al/Fe] – [Mg/Fe] abundance ratios and follow distinct sequences in the age–[Fe/H] plane. The *in-situ* GCs in our classification show a clear disc spin-up signature – the increase of median  $V_{\phi}$  at metallicities -1.3 < [Fe/H] < -1 similar to the spin-up in the *in-situ* field stars. This signature signals the MW's disc formation, which occurred  $\approx 11.7-12.7$  Gyr ago (or at  $z \approx 3.1-5.3$ ) according to *in-situ* GC ages. *In-situ* GCs with metallicities of  $[Fe/H] \gtrsim -1.3$  were thus born in the MW disc, while lower metallicity *in-situ* GCs were born during early, turbulent, pre-disc stages of the evolution of the Galaxy and are part of its Aurora stellar component.

**Key words:** stars: kinematics and dynamics—Galaxy: abundances—Galaxy: globular clusters—Galaxy: evolution—Galaxy: formation—Galaxy: structure.

## 1 INTRODUCTION

The Milky Way offers an uninterrupted view of the time evolution of a single galaxy, thus providing us with a useful benchmark for the theory of galaxy formation (e.g. see Bland-Hawthorn & Gerhard 2016, for a review). In the hierarchical structure formation scenario (Peebles 1965; Peebles & Yu 1970), galaxy evolution is driven by the formation of in-situ stars in the main progenitor (Eggen, Lynden-Bell & Sandage 1962) and accretion of stars from the smaller galaxies that merge with it (Searle 1977). Globular clusters (GCs) have long been used to elucidate the early phases of the Milky Way's formation, in particular the relative importance of the in-situ formation and the accretion of sub-galactic fragments (e.g. Searle & Zinn 1978; Côté et al. 2000; Forbes & Bridges 2010; Leaman, VandenBerg & Mendel 2013; Myeong et al. 2018; Massari, Koppelman & Helmi 2019). However, the origin of clusters themselves was until recently rather uncertain, with ideas of their formation spanning from the Jeans fragmentation in the early intergalactic medium (Peebles & Dicke 1968), formation predominantly in the cores of dwarf galaxies (Searle & Zinn 1978; Peebles 1984), thermal instability in the halo gas of the MW progenitor (Fall & Rees 1985), gas compressions due

to shocks in the primordial molecular clouds (Gunn 1980; Murray & Lin 1992; Harris & Pudritz 1994; Burkert, Brown & Truran 1996), gas compression produced during major mergers (Schweizer 1987; Ashman & Zepf 1992, 2001).

Our understanding of globular cluster formation was revolutionized by the high-resolution observations with the *Hubble Space Telescope (HST)*. Early *HST* observations confirmed efficient formation of compact GC-like objects in merging galaxies during their final galaxy collision stage (e.g. Whitmore et al. 1993; Whitmore & Schweizer 1995; Holtzman et al. 1996; Whitmore et al. 1999; Zepf et al. 1999). However, subsequent observations of a wider range of galaxies showed that globular clusters form as part of regular star formation in galaxies where gas and star formation surface densities are sufficiently large (e.g. see Krumholz, McKee & Bland-Hawthorn 2019; Adamo et al. 2020, for reviews).

Indeed, models in which GC formation was implemented as part of a regular star formation during gas-rich phases of galaxy evolution in the hierarchical cosmological framework have proved quite successful in matching basic observed properties of GC populations (e.g. Côté et al. 2000; Beasley et al. 2002; Côté, West & Marzke 2002; Kravtsov & Gnedin 2005; Muratov & Gnedin 2010; Kruijssen 2015; Choksi, Gnedin & Li 2018; Choksi & Gnedin 2019; Kruijssen et al. 2019b; Chen & Gnedin 2022; Reina-Campos et al. 2022b; Chen & Gnedin 2023), although some discrepancies still remain, for example

Downloaded from https://academic.oup.com/mnras/article/528/2/3198/7485911 by guest on 20 December 2024

<sup>&</sup>lt;sup>4</sup>Enrico Fermi Institute, The University of Chicago, Chicago, IL 60637, USA

<sup>\*</sup> E-mail: vasily@ast.cam.ac.uk (VB); kravtsov@uchicago.edu (AK)

in Reina-Campos et al. (2019) model GCs are systematically younger compared to observations. It is thus now generally acknowledged that GCs are tracing star formation in galaxies, albeit at specific epochs when conditions conducive for their formation exist (e.g. Kruijssen 2015; Choksi, Gnedin & Li 2018; Reina-Campos et al. 2022b). Thus, for example, the Milky Way has not been forming globular clusters for the past  $\sim 8-10$  Gyrs, while it formed most of its *in-situ* stellar population during these epochs.

Furthermore, the number of GCs scales approximately linearly with the total halo mass (see Spitler & Forbes 2009; Hudson, Harris & Harris 2014; Harris, Blakeslee & Harris 2017; Forbes et al. 2018; Burkert & Forbes 2020; Dornan & Harris 2023), while stellar mass of galaxies with luminosities  $L \leq L_{\star}$  scales much faster,  $M_{\star} \propto M_{\rm h}^{\alpha}$  where  $\alpha \approx 1.5-2.5$  depending on  $M_{\star}$  (e.g. Kravtsov, Vikhlinin & Meshcheryakov 2018; Nadler et al. 2020). This means that the number of GCs per stellar mass increases with decreasing  $M_{\star}$  and accreted dwarf galaxies contribute proportionally more GCs to the host galaxy than field stars.

In the Milky Way globular cluster formation is biased towards earlier epochs when its main progenitor experienced larger accretion and merger rates and was generally considerably more gas-rich. GCs can thus be a useful probe of the Galaxy evolution and merger history during these early epochs. However, this requires a way to differentiate GCs that were born *in-situ* in the main MW progenitor and GCs that were accreted as part of other galaxies. The earliest efforts to identify accreted and *in-situ* clusters were based on the metallicity and spatial distribution of GCs. Zinn (1985, see also Zinn 1996 for review) divided clusters by metallicity at [Fe/H] = -0.8 and argued that such division resulted in GC populations with distinct spatial and kinematic properties. For example, it was claimed that the metal-richer Galactic GCs likely originated in the MW disc as supported by the small scale height of their vertical distribution and a substantial rotational velocity (Zinn 1985).

The existence of a significant population of disc GCs gives us a chance to pin down the epoch of formation of the MW disc. When reliable cluster ages have become available, a number of studies used GC distribution in the age-metallicity (AM) plane and their chemical element ratios to identify *in-situ* and accreted sub-populations (Marín-Franch et al. 2009; Forbes & Bridges 2010; Leaman, VandenBerg & Mendel 2013; Recio-Blanco 2018). In particular, these studies demonstrated the existence of two distinct AM sequences: a shallower one corresponding to older *in-situ* GCs and a steeper one containing younger clusters that were argued to be accreted with other galaxies. Following the works by e.g. Zinn (1985) and Dinescu, Girard & van Altena (1999), Leaman, VandenBerg & Mendel (2013) identified a number of old *in-situ* GCs with disc-like kinematics.

Earlier studies used available kinematic information to aid insitu/accreted classification (e.g. Dinescu, Girard & van Altena 1999), but such information was quite limited until the advent of the Gaia satellite (Gaia Collaboration et al. 2016). Inspired by ideas proposed by Helmi & de Zeeuw (2000), Myeong et al. (2018) were the first to use GC orbital properties based on the Gaia Data Release 2 astrometry to identify a large group of clusters accreted together. Subsequently, Massari, Koppelman & Helmi (2019) relied on distributions of GCs in the age-metallicity plane as guidance to come up with a number of criteria that use spatial distribution and kinematical properties of GCs measured by Gaia to classify almost all of the MW GCs into *in-situ* and accreted subpopulations. Some of their criteria relied on traditional cuts used in previous studies, such as a cut on the maximum Z coordinate to identify 'disc' clusters. Although reasonable, such criteria left a significant fraction of clusters with ambiguous/uncertain classification and these

clusters were putatively assigned to new accreted structures (e.g. the 'low-energy group') or known dwarf galaxies or streams. Some of these GCs were also argued to be a remnant of the putative massive dwarf galaxy that merged with the MW progenitor around z > 2(Kruijssen et al. 2019b, 2020). Thus, similarly to the early studies, in the recent classification attempts, a large fraction of the lowmetallicity GCs with non-disc kinematics has been attributed to the accreted halo. Lately, there have also been attempts to re-assess some of the principles on which the above classification schemes are based. For example, Callingham et al. (2022) propose to use a more objective approach using a multi-component mixture model instead. More drastically, Pagnini et al. (2023) argue that tidal debris from massive mergers can sink and radialize (see Vasiliev, Belokurov & Evans 2022) in the host galaxy to create a pile-up of GCs in integrals-of-motion space, thus rendering individual accretion events indistinguishable.

Most recently, it was realized that *in-situ* born stars and stars in dwarf galaxies are distinct in their distributions of the aluminium-to-iron, [Al/Fe], and sodium-to-iron ratios (Hawkins et al. 2015; Das, Hawkins & Jofré 2020). We used this finding in Belokurov & Kravtsov (2022) and Belokurov & Kravtsov (2023) to identify and study kinematic and chemical properties of the MW's *in-situ* stellar and GCs populations. The latter study showed that [Al/Fe]-based classification at intermediate metallicites results in a fairly distinct distribution of the *in-situ* and accreted stars and GCs in the space of total energy E and  $L_z$  angular momentum and this can be used in the *in-situ*/accreted classification of the entire stellar and GC populations (see Horta et al. 2020, for comparison). Note that the classification proposed by Belokurov & Kravtsov (2023) is not dissimilar to the idea of the 'critical energy' introduced in Myeong et al. (2018) to segregate Galactic GCs into distinct groups.

In this study we use the [Al/Fe]-calibrated *in-situ*/accreted classification in the  $E-L_z$  plane to demonstrate that such classification results in the GC populations with distinct spatial, kinematic and chemical abundance distributions. We also show that the *in-situ* GCs in this classification show a clear disc spin-up signature (a rapid, high-amplitude increase in the median azimuthal velocity) that signals MW's disc formation and which was previously identified in the *in-situ* stars.

The paper is organized as follows. In Section 2, we describe the sample of GCs and their properties assembled from different sources. In Section 3, we summarize the in-situ/classification method of Belokurov & Kravtsov (2023) and its underpinnings. We present distributions and statistics of the classified in-situ and accreted GC populations in Section 4 and discuss differences from previous classification schemes in Section 5. We summarize our results and conclusions in Section 6. Finally, in the Appendix A we describe the data on chemical abundances from the literature that was used to complement APOGEE measurements. The Appendix B presents results of the FIRE-2 simulations demonstrating the boundary between accretion and in-situ-dominated regions in the energyangular momentum plane. Appendix C describes an alternative way to measure the spin-up metallicity of GCs using a functional fit to the individual  $V_{\phi}$  and [Fe/H] of clusters. Finally, Appendix D presents the table of the MW GCs with in-situ/accreted classifications according to the method presented in this paper.

# 2 SAMPLE OF THE MILKY WAY GLOBULAR CLUSTERS

Our globular cluster catalogue is based on the 4th version of the GC database assembled by Holger Baumgardt. More specifically,

we use (i) the table with masses and structural parameters<sup>1</sup> and (ii) the table with GC kinematics and orbital parameters<sup>2</sup>, the latter table is used not only for the GCs' phase-space coordinates but also for the orbital eccentricities (computed with the published pericentric and apo-centric distances). The resulting catalogue, once the two tables are cross-matched and merged, contains 165 Milky Way GCs.

Mean cluster motions are based on Gaia EDR3 (Gaia Collaboration 2021; Lindegren et al. 2021) data (see Vasiliev & Baumgardt 2021 for details on the analysis of the *Gaia* EDR3 data). This version uses the *V*-band luminosities derived in Baumgardt, Sollima & Hilker (2020) and the GC distances derived in Baumgardt & Vasiliev (2021). Details of *N*-body models are described in Baumgardt (2017) and Baumgardt & Hilker (2018). Details on the stellar mass functions can be found in Baumgardt et al. (2023).

The catalogue is augmented with metallicities published by Harris (2010) and other literature sources. GC ages used in this study are from VandenBerg et al. (2013) who build a homogeneous sample of age measurements based on HST photometry. We note however, that the cluster age and metallicity measurements in the VandenBerg et al. (2013) sample do not show the *in-situ* and accreted GC branches as distinct as the measurements in e.g. the Forbes & Bridges (2010) compilation. Total energy and the vertical component of the angular momentum  $L_z$  for individual clusters used in the in-situ/accreted classification below are computed using the assumptions about the Galaxy described in the beginning of Section 2 of Belokurov et al. (2023). The GCs in our catalogues are matched by name to 160 objects with tentative progenitor hosts published by Massari, Koppelman & Helmi (2019). Five objects published by Massari, Koppelman & Helmi (2019), namely Koposov 1, Koposov 2, BH 176, GLIMPSE 1 and GLIMPSE 2 are omitted. GLIMPSE 1 and GLIMPSE 2 are highly extincted and thus their properties are not constrained. Koposov 1, Koposov 2, and BH 176 may be misclassified open clusters (see Davoust, Sharina & Donzelli 2011; Paust, Wilson & van Belle 2014). Therefore, only 155 out of 165 GCs in our catalogue have progenitor assignments in Massari, Koppelman & Helmi (2019).

# 3 CLASSIFICATION OF ACCRETED AND IN-SITU STARS AND CLUSTERS

Our method of classification of GCs and MW stars into *in-situ* and accreted clusters was presented in Belokurov & Kravtsov (2023). Here, we review the key details of the method relevant for this study.

The method is based on classification of stars and clusters using the [Al/Fe] ratio. Hawkins et al. (2015) showed that [Al/Fe] have very different typical values in dwarf galaxies and in the Milky Way and argued that this difference can be used to distinguish the accreted and *in-situ* halo components (see also Das, Hawkins & Jofré 2020). The difference arises because Al yield has a strong metallicity dependence and MW progenitor and dwarf galaxies that merge with it and contribute stars to the accreted halo component evolve at very different rates (see e.g. Kobayashi et al. 2006). The MW progenitor evolves fast and reaches metallicities required for efficient Al production much earlier than dwarf galaxies that form

their stellar population at a much slower pace. As a result, stars born in the Milky Way exhibit a rapid increase in [Al/Fe] around  $-1.5 < [{\rm Fe/H}] < -0.9$  and there is a gap in the Al abundance at the same [Fe/H] between MW progenitor and dwarf galaxies that merge with it

We use this fact as the basis for our classification. Specifically, BK22 classify stars with APOGEE's [Al/Fe] >-0.075 as in-situ and those with [Al/Fe] <-0.075 as accreted, which is supported by the fact that the observed surviving massive MW dwarf satellites typically have [Al/Fe] <-0.1 (Hasselquist et al. 2021). At metallicities [Fe/H]  $\lesssim-1.5$  the difference in typical values of [Al/Fe] between MW progenitor and accreted dwarfs becomes small and a clear [Al/Fe]-based classification becomes unreliable. Our classification is thus based on a two-step approach.

In the first step, we use the [Al/Fe]-based classification in the metallicity range -1.4 < [Fe/H] < -1.1, where it is most reliable, with the threshold separating in-situ and accreted clusters assumed to be [Al/Fe] = -0.075. As shown in fig. 2 of Belokurov & Kravtsov (2023, see also discussion in their section 3.2) the in-situ and accreted components classified in this way, separate quite well in the plane of total energy E and the z-component of the angular momentum  $L_z$ . This separation can be well described by the following  $L_z\text{-}dependent$  boundary in energy:

$$L_z < -0.58$$
:  $E = -1.3$ ,  
 $-0.58 < L_z < 0.58$ :  $E = -1.4 + 0.3L_z^2$ ,  
 $L_z > 0.58$ :  $E = -1.325 + 0.075L_z^2$ , (1)

where E is in units of  $10^5 \, \mathrm{km^2 \, s^{-2}}$  and  $L_z$  is in units of  $10^3 \, \mathrm{kpc \, kms^{-1}}$ . It is worth noting that although the form of this boundary is derived as an accurate empirical approximation to the boundary between regions of the  $E-L_z$  space dominated by the *in-situ* and accreted populations in the [Al/Fe]-based classification, a qualitatively similar boundary shape among the regions of the  $E-L_z$  space that is dominated by these components is found in the FIRE-2 simulations of MW-sized galaxies (see Appendix B).

In Belokurov & Kravtsov (2023), we showed that this boundary does a good job of separating objects into *in-situ* and accreted components with a high accuracy ( $\gtrsim$  95 per cent) comparable to the classification accuracy achievable with the best machine learning algorithms. Moreover, we have also tested that adding metallicity or Galactocentric distance to the classification with machine learning methods does not improve the accuracy.

Although this boundary is obtained using [Al/Fe] ratio within a limited range of metallicities, we assume that the same boundary  $E_{\rm bound}(L_z)$  is applicable in the entire metallicity range. Therefore in the second step, all GCs with total energies below the  $E_{\rm bound}(L_z)$  boundary defined in equation (1) are classified as in-situ and those above as accreted. Fig. 1 shows E and  $L_z$  distributions of the MW GCs classified as accreted (red) and in-situ (blue) along with the boundary  $E_{\rm bound}(L_z)$  used for classification. A sizeable fraction of the accreted GCs were likely brought into the MW during the Gaia Sausage/Enceladus event (GS/E, Belokurov et al. 2018; Helmi et al. 2018; Myeong et al. 2018). In what follows, we examine distribution of various GC properties in the components classified using the boundary shown in Fig. 1.

Out of 164 Galactic GCs with measured metallicities (BH 140 does not have a metallicity estimate currently) considered in this study, 106, or  $\approx$ 2/3 are classified as *in-situ* and 58 as accreted. Classification for individual clusters is presented in the Table D1 in Appendix D.

<sup>&</sup>lt;sup>1</sup>See https://people.smp.uq.edu.au/HolgerBaumgardt/globular/parameter.html.

 $<sup>{}^2</sup> See \quad https://people.smp.uq.edu.au/HolgerBaumgardt/globular/orbits\_table. \\ txt.$ 

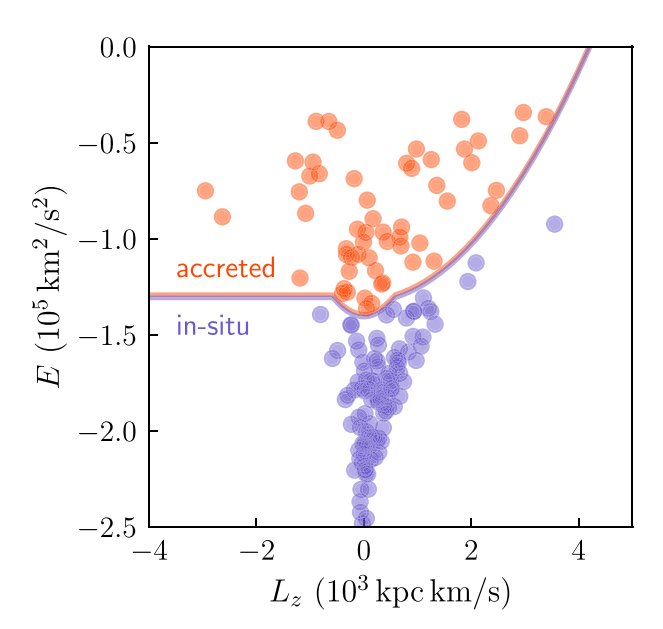


**Figure 1.** Distribution of the 165 MW GCs in the plane of total energy E and angular momentum  $L_z$ . The line indicates the boundary separating the *in-situ* clusters (blue/purple) below the line and accreted clusters (red/orange) above the line.

### 4 RESULTS

In what follows we will consider distributions of various properties of the *in-situ* and accreted GCs in our classification from their spatial distributions to the distributions of their metallicity, age, and kinematic properties.

### 4.1 Spatial distribution

Fig. 2 shows spatial distribution of the *in-situ* (blue/purple) and accreted (red/orange) MW GCs classified using method described above in Section 3 (see Fig. 1). The left panel shows the absolute value of z coordinate (in the coordinate system where MW disc is in the x-y plane) as a function of galactocentric distance in the disc plane  $R = (x^2 + y^2)^{1/2}$ . It shows clearly that the two populations are well segregated in both z and R with most of the *in-situ* classified clusters located at |z| < 3 kpc and R < 10 kpc. The distribution of the accreted clusters, on the other hand, is much more extended. Although one could argue that such segregation is largely defined by the fact that classification of clusters is done using total energy boundary, the fact that the *in-situ* clusters have different |z| and R ranges shows that it does not simply classify clusters within a given limiting galactocentric distance.

Indeed, as can be seen in the middle panel of Fig. 2 the distribution of in-situ clusters is quite flattened in the z-direction around the x-y plane of the MW disc. The distribution of the accreted clusters, on the other hand, is fairly isotropic. The right panel does not show a similar flattening in the in-situ GC distribution in the x-y projection indicating that it can be characterized as an oblate ellipsoid or a thick disc. As we will discuss below in Section 4.5, the discy flattened distribution is even more pronounced for the in-situ clusters with [Fe/H] > -1.

The figure shows that the two classified populations have very distinct spatial distributions. Notably, similar two populations are identified if we use the OPTICS clustering algorithm (Ankerst

et al. 1999) and reachability curves<sup>3</sup> to identify clusters in the 3D distribution of GCs, which again indicates good segregation of the *in-situ* and accreted populations in space.

### 4.2 Distribution in the age-[Fe/H] plane

Fig. 3 shows distributions of the *in-situ* (blue) and accreted (red) MW GCs in the age-metallicity plane using clusters that have age estimates (VandenBerg et al. 2013). The circles show the individual GCs, while the lines are the median of the binned distributions obtained using different radial range for bin placement. This is done to estimate the effect of bin placement choice on the result. Specifically, we shift all bin edges to the right in small increments from their original locations up to the shift equal to the bin size and reconstruct histograms for the new edges. We then estimate the median of all the histograms obtained for individual shifts and 68 per cent region of histograms around the median.

The figure shows that our classification in the total energy and angular momentum  $L_z$  selects distinct sequences of clusters in the age–metallicity plane with a rather small overlap. The *in-situ* clusters are predominantly older by 0.5 Gyr at a given metallicity for  $[Fe/H] \lesssim -1.5$  and by  $\gtrsim 1$  Gyr at larger metallicities. Conversely, the *in-situ* clusters have larger metallicities by  $\approx 0.3-0.5$  dex at a given age. The two sequences overlap somewhat only for the oldest and lowest metallicity clusters.

The two sequences in the age-metallicity space identified by our classification in the  $E-L_z$  plane were identified previously (see discussion in e.g. Forbes & Bridges 2010). Notably, Leaman, VandenBerg & Mendel (2013) identified a clear sequence of GCs born with disc-like kinematics down to  $[Fe/H] \approx -1.3$  (see also Recio-Blanco 2018). As we discuss below, the kinematics of these GCs is consistent with their disc origin. Our classification shows that these clusters are a part of the 'in-situ sequence' that extends to metallicities of  $[Fe/H] \approx -2.3$ . This is consistent with the model-based interpretation of Kruijssen et al. (2019a).

It is worth noting that the *in-situ* sequence in Fig. 3 has a sharp turnover to lower ages at  $[Fe/H] \approx -1$ . Although this metallicity is similar to the metallicity of the disc spin-up that we will discuss below, this turnover is likely not directly related to disc formation but reflects the general form of the age—metallicity relation of MW-sized galaxies. Indeed, galaxy formation models generally predict such turnover exactly at  $[Fe/H] \approx -1$  (see e.g. the middle panel of fig. 14 in BK22), which marks the transition from the fast to slow mass accretion regime of evolution.

The grey-shaded vertical rectangular area in the figure shows the range of metallicities -1.3 < [Fe/H] < -0.9 which corresponds to the disc spin-up exhibited by the *in-situ* MW stars estimated in BK22. As shown in BK22, before the spin-up the average angular momentum of Galaxy's stellar populations is low; during the spin-up phase the median azimuthal velocity increases rapidly to high values (see also Chandra et al. 2023; Semenov et al. 2023; Dillamore et al. 2024). The horizontal gray rectangular area shows the corresponding approximate range of cluster ages of  $\approx 11.7-12.7$  Gyr (i.e. lookback spin-up time) consistent with the estimate of Conroy et al. (2022). This range of disc formation lookback times corresponds to the range of redshifts  $z \approx 3.07-5.3$  for the Planck cosmology. Although this

<sup>&</sup>lt;sup>3</sup>For examples of application of the OPTICS algorithm see https://scikit-learn.org/stable/auto\_examples/cluster/plot\_optics.html.

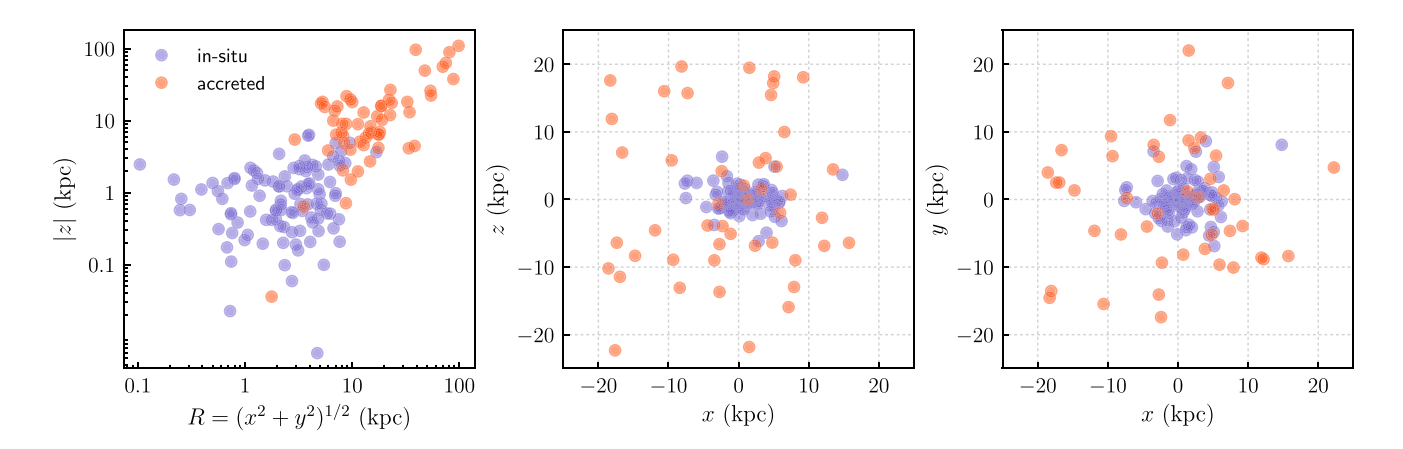


**Figure 2.** Spatial distribution of the *in-situ* (blue) and accreted (red) MW GCs classified using method described in Section 3 (see Fig. 1). The left panel shows the absolute value of z coordinate (in the coordinate system where MW disc is in the x-y plane) as a fraction of galactocentric distance in the disc plane  $R = (x^2 + y^2)^{1/2}$ . The middle and right panels show spatial distributions of the *in-situ* and accreted GCs in the x-z and x-y plane. The figure shows that the two populations have very distinct spatial distributions. Note that the distribution of the accreted clusters is fairly isotropic, while the distribution of *in-situ* clusters is flattened around the x-y plane of the MW disc.

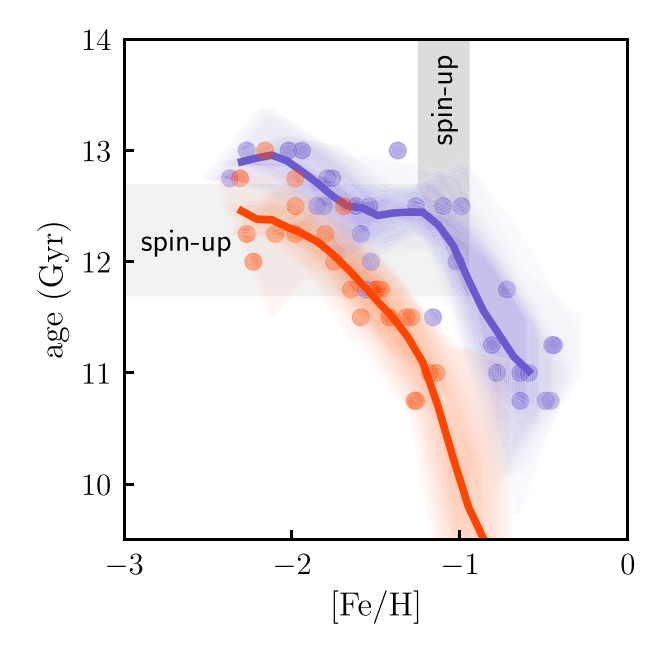


**Figure 3.** Distribution of 54 MW GCs classified as *in-situ* (blue) and accreted (red) by our classification method that have age and [Fe/H] estimates by VandenBerg et al. (2013). The circles show the individual GCs, while the lines are the median of the binned distributions (see the text for details). The shaded rectangular areas indicate the spin-up range of metallicities and the corresponding approximate range of the stellar age (i.e. lookback spin-up time).

range is fairly broad, the result indicates that Milky Way formed its disc earlier than a typical galaxy of similar stellar mass both in observations (Simons et al. 2017) and galaxy formation simulations (Belokurov & Kravtsov 2022; Semenov et al. 2023; Dillamore et al. 2024).

## 4.3 Metallicity distributions of in-situ and accreted GCs

Metallicity distributions of the *in-situ* and accreted GCs are shown in Fig. 4 along with the metallicity distribution of the entire GC sample.

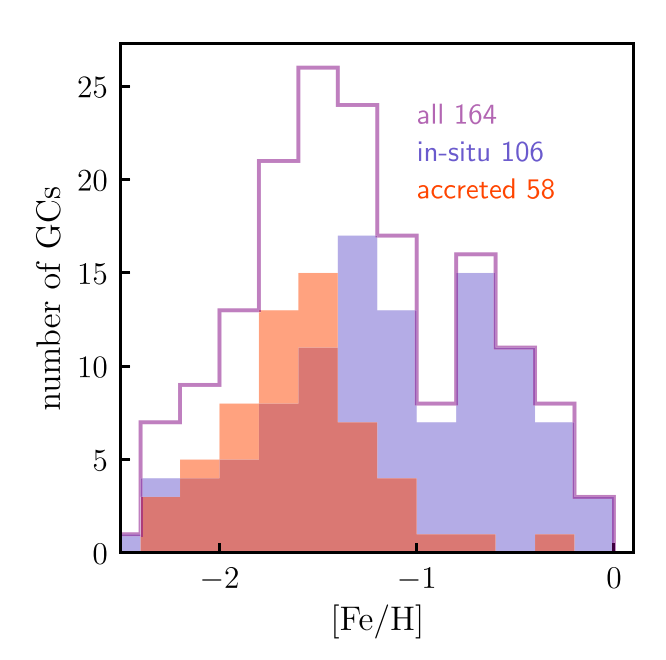


**Figure 4.** Distribution of [Fe/H] of the MW GCs (solid magenta histogram), *in-situ* GCs (blue histogram) and accreted GCs (red histogram) in our classification. Note that bimodality in the metallicity distribution is only present in the *in-situ* GCs.

The distributions of the *in-situ* and accreted GCs in our classification are clearly different with accreted GCs having mostly metallicities [Fe/H] < -1. At the same time, at these low metallicities there is a significant overlap of the accreted and *in-situ* clusters and they clearly do not separate neatly in metallicity, as envisioned in the classification of Zinn (1985).

Remarkably, Fig. 4 shows that only the distribution of *in-situ* GC metallicities is bimodal, while accreted clusters have a distribution with a single peak at [Fe/H] < -1.6. The origin of the bi-modality in the metallicity distribution is still debated. Traditionally, bimodality is thought to be produced by a combination of metallicity evolution of

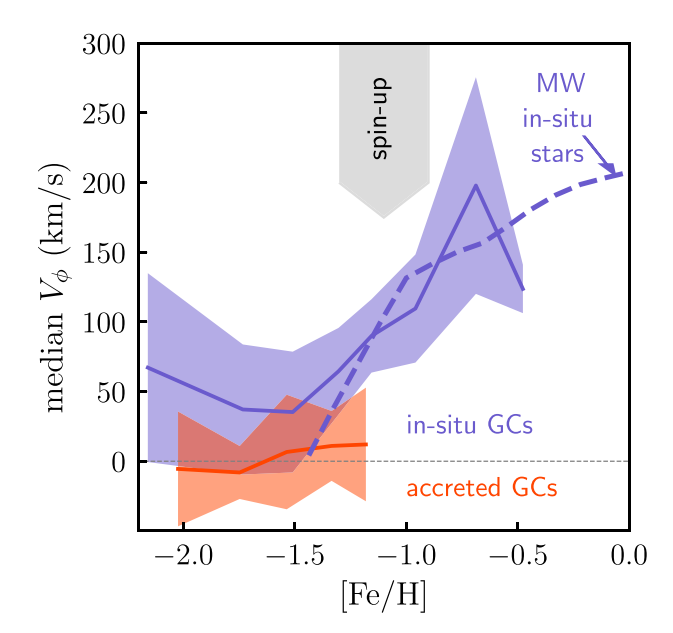


Figure 5. Tangential velocity of the *in-situ* (blue) and accreted (red) GCs as a function of their metallicity [Fe/H]. The solid lines show the median of the bootstrap resamples of the original GC sample, while shaded areas show their  $1\sigma$  scatter. The dashed line shows the corresponding median  $V_{\phi}$  as a function of metallicity for the *in-situ* MW stars, as estimated by (Belokurov & Kravtsov 2022). Downward gray arrow indicates the range of metallicities in which MW disc spin-up was identified for these stars. The figure shows that the *in-situ* MW GCs in our classification also exhibit a clear spin-up feature at the same metallicity range of [Fe/H]  $\in$  [-1.3, -0.9] as the *in-situ* stars.

galaxies and gas-rich mergers (e.g. Ashman & Zepf 1992; Muratov & Gnedin 2010; Li & Gnedin 2014; Valenzuela et al. 2023).

The gas-rich mergers can of course also imprint bimodality in the *in-situ* GC population by inducing a starburst in the MW progenitor. However, such bi-modality may be imprinted in the [Fe/H] distribution even without mergers by the same transition from the fast to slow mass accretion regime that produces the sharp turnover in the age–[Fe/H] sequence of the *in-situ* clusters discussed above. After the Galaxy transitions to the slow accretion regime at [Fe/H]  $\approx -1$  clusters born with a broad range of ages have similar metallicities, which creates a peak at high metallicities (see El-Badry et al. 2019). Conversely, clusters born during the early fast accretion regime have a narrow range of ages and broad distribution of metallicities, which peaks at metallicities corresponding to the time when the MW progenitor's star formation rate was at its maximum.

#### 4.4 Milky Way disc spin-up traced by in-situ GCs

Fig.5 shows the tangential velocity of the *in-situ* (blue) and accreted (red) GCs as a function of their metallicity [Fe/H]. The solid lines show the median of the bootstrap resamples of the original GC sample, while shaded areas show their  $1\sigma$  scatter. The dashed line shows the corresponding median  $V_{\phi}$  as a function of metallicity for the *in-situ* MW stars, as estimated by Belokurov & Kravtsov (2022). Although the number of clusters per bin is fairly small and exact form of the median  $V_{\phi}$  curve depends on the number of bins used, in the Appendix C we show that a similar result is obtained if a parametric 'soft step' function is fit to the distribution of individual [Fe/H] and  $V_{\phi}$  values.

The figure shows that the *in-situ* MW GCs in our classification also exhibit a clear spin-up feature at the same metallicity range of  $[Fe/H] \in [-1.3, -0.9]$  as the *in-situ* stars of the Milky Way. The fact that metal-rich 'disc' GCs ([Fe/H] > -0.8 in the Zinn 1985 classification) exhibit large net rotation is well known (Armandroff 1989). Fig. 5, however, shows that the process of the MW disc formation is imprinted in its *in-situ* GC population at metallicities  $[Fe/H] \gtrsim -1.3$ . This implies the *in-situ* GCs at this wide range of metallicities were formed in the MW disc after its formation and retained corresponding kinematics (see also Leaman, VandenBerg & Mendel 2013; Recio-Blanco 2018).

Conversely, the *in-situ* GCs with metallicities [Fe/H] < -1.3 were born during turbulent pre-disc stages of MW evolution and are thus a part of the *Aurora* stellar component of the Galaxy identified in Belokurov & Kravtsov (2022, see also Conroy et al. 2022; Rix et al. 2022). Interestingly, the Aurora clusters show net rotation with the median  $V_{\phi} \approx 50$  km/s. This net velocity is similar to the typical median velocity of the *in-situ* stars at the pre-disc metallicites in simulations of MW-sized galaxies (Belokurov & Kravtsov 2022; Semenov et al. 2023; Dillamore et al. 2024). However, the non-zero median  $V_{\phi}$  does not imply that these stars and GCs were born in a disc. In fact, they were generally born in very chaotic configurations (see fig. 10 in Belokurov & Kravtsov 2022). Nor does it necessarily mean that GCs were born with such net rotation. As shown by Dillamore et al. (2023), its origin maybe in the trapping of these old GCs by rotating bar that forms during latter stages of the MW disc evolution.

Fig. 6 shows distributions of the tangential velocity  $V_{\phi}$  for the in-situ (blue) and accreted (red) MW GCs. The upper panel shows distribution for the low-metallicity GCs with [Fe/H] < -1, while the lower panel shows the distribution for GCs with [Fe/H] > -1. The figure shows that  $V_{\phi}$  distributions of low- and high-metallicity clusters are quite different. The distribution for the low-metallicity clusters has a single peak, with that of the accreted clusters centered at  $V_{\phi} \approx 0 \text{ km s}^{-1}$ , while distribution for the in-situ clusters centered at  $V_{\phi} \approx 50 \text{ km s}^{-1}$  as noted above.

The  $V_{\phi}$  distribution of the high-metallicity *in-situ* clusters is very skewed with a significant fraction of clusters coherently rotating with  $V_{\phi} \sim 200~{\rm km~s^{-1}}$ , while a tail of the *in-situ* GCs has  $V_{\phi} \lesssim 0$ . Note that  $V_{\phi}$  distributions of the low- and high-metallicity *in-situ* GCs is very similar to the distribution of tangential velocities of the MW's *in-situ* stars in fig. 6 of Belokurov & Kravtsov (2022) at similar metallicities. In particular, *in-situ* stars also exhibit a tail towards  $V_{\phi} < 0$  and a similar tail can be seen in the distribution of *in-situ* stars in simulations of the MW-sized galaxies (see Appendix B).

Finally, Fig. 7 shows velocity anisotropy defined as

$$\beta = 1 - \frac{\sigma_{\phi}^2 + \sigma_{\theta}^2}{2\sigma_r^2} \tag{2}$$

as a function of metallicity [Fe/H] for the accreted (red) and *in-situ* (blue) GCs. Different lines correspond to the estimates obtained using different placements of the metallicity bins in the range spanned by the GCs. It shows that velocity anisotropy of the accreted clusters is close to isotropic at the lowest metallicity and has a moderate radial anisotropy at metallicities [Fe/H]  $\approx -1.7 \div -0.7$ . The *in-situ* GCs, on the other hand, have a nearly isotropic velocity distribution at [Fe/H]  $\lesssim -1.3$ , but the distribution changes sharply at lower metallicities where the distribution has a clear tangential anisotropy.

<sup>&</sup>lt;sup>4</sup>Named after Aurora – the Latin name of the goddess of dawn Eos in Greek mythology.

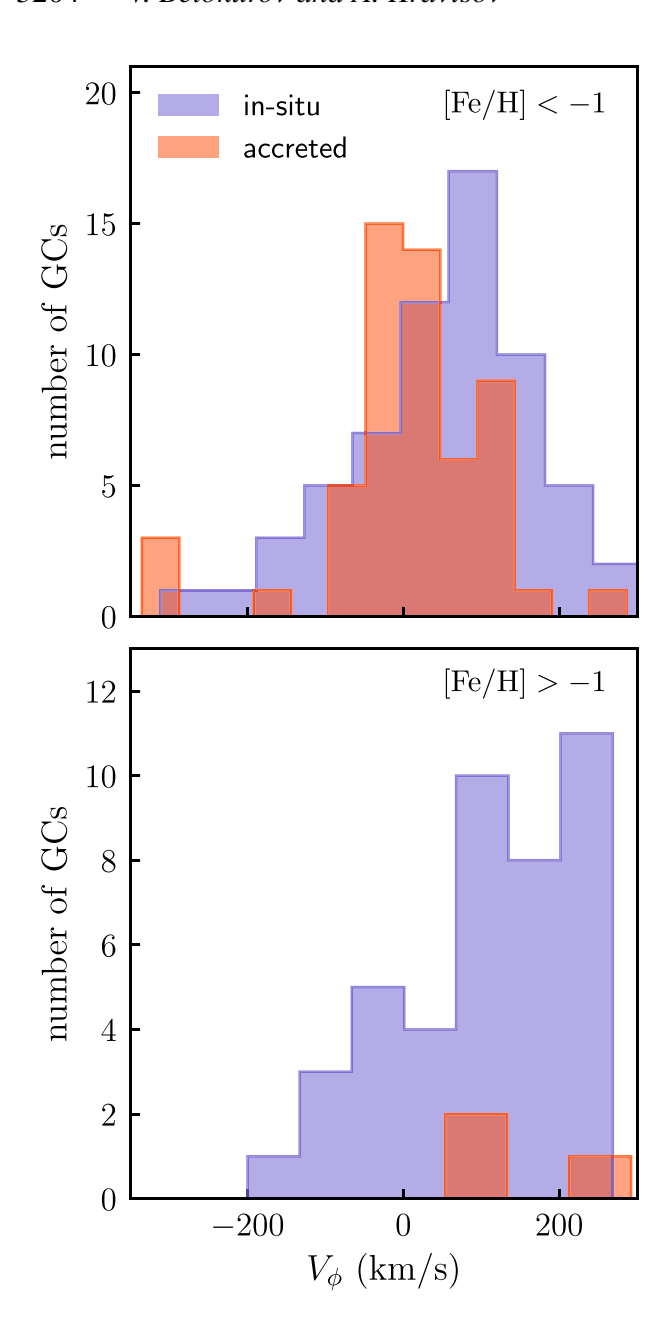


**Figure 6.** Distributions of the tangential velocity  $V_{\phi}$  for the *in-situ* (blue) and accreted (red) MW GCs. The upper panel shows distribution for the low-metallicity GCs with [Fe/H] < -1, while the lower panel shows the distribution for GCs with [Fe/H] > -1. The figure shows that  $V_{\phi}$  distributions of low- and high-metallicity clusters are quite different. Distribution for the low-metallicity clusters has a single peak, with that of the accreted clusters centred at  $V_{\phi} \approx 0$  km s<sup>-1</sup>, while distribution for the *in-situ* clusters centered at  $V_{\phi} \approx 50$  km s<sup>-1</sup>. The  $V_{\phi}$  distribution of the high-metallicity *in-situ* clusters is very skewed with a significant fraction of clusters coherently rotating with  $V_{\phi} \sim 200$  km s<sup>-1</sup>, while a tail of the *in-situ* GCs has  $V_{\phi} \lesssim 0$  km s<sup>-1</sup>.

# 4.5 Comparisons of the low- and high-metallicity *in-situ* clusters

Given qualitative changes that MW progenitor clearly underwent at [Fe/H] = -1 both due to the transition from the fast to slow mass accretion regime and due to the formation of the disc, it is interesting to consider differences in properties of the *in-situ* 

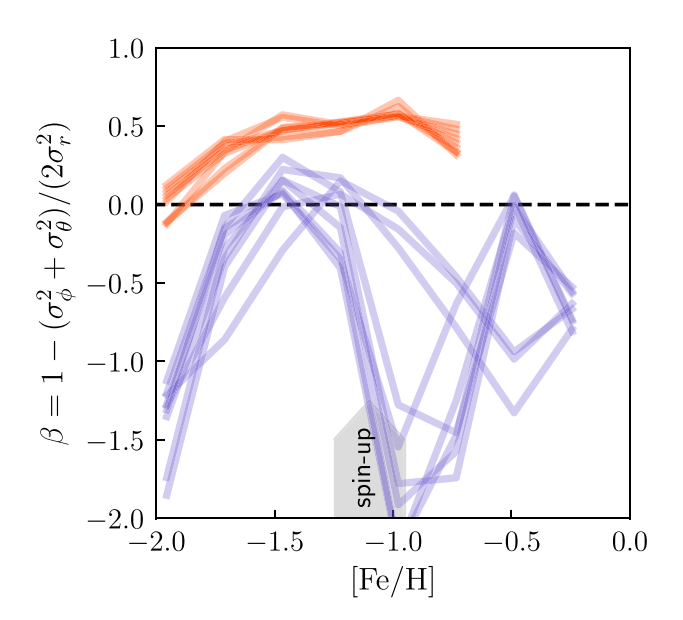


**Figure 7.** Velocity anisotropy of the MW GCs defined as  $\beta=1-(\sigma_\phi^2+\sigma_\phi^2)/(2\sigma_r^2)$  as a function of metallicity [Fe/H] for the accreted (red) and *insitu* (blue) GCs. Different lines correspond to the estimates obtained using different placement of metallicity bins in the range of metallicities spanned by the GCs.

GCs with [Fe/H] < -1 and [Fe/H] > -1 straddling this transition metallicity.

Fig. 8 shows the x-z, x-y, and y-z projections of the spatial distribution of *in-situ* GCs with metallicities [Fe/H] <-1 and [Fe/H] >-1. The figure shows that the distribution of high-metallicity *in-situ* GCs is somewhat more flattened around the z=0 plane than the distribution of low-metallicity clusters consistent with their formation in the disc.

Interestingly, we also find that 11 clusters in the metallicity range of the first peak in the metallicity distribution -1.5 < [Fe/H] < -1.3(shows as dark purple points) are distributed in a rather narrow filament or prolate ellipsoid with a small c/a axes ratio. Although the number of objects is too small to make definitive conclusions, we speculate that the formation of these clusters could have been induced in the MW progenitor by the tidal forces and/or gas accretion associated with the early stages of the GS/E merger. This process thus could be responsible for both an overall burst of star formation in the MW progenitor and burst of GC formation that produced the low-metallicity peak in the metallicity distribution of in-situ clusters (see Fig. 4). Indeed, one can generally expect that the maximum initial mass of the forming GCs scales with star formation rate (Maschberger & Kroupa 2007) and initial insitu GC masses estimated by Baumgardt & Makino (2003) at metallicities  $-1.5 \lesssim [\text{Fe/H}] \lesssim -1.3$  do reach values of  $\log_{10} M_{\text{ini}}$ > 6.5 larger than maximum initial masses for neighbouring metallicity ranges. In fact, all of the other MW GCs with such large masses are among in-situ clusters at [Fe/H] > -1 near the second peak in their metallicity distribution. It is also notable that accreted GCs do not show such increased maximum  $M_{\rm ini}$  at any metallicity.

Fig. 9 shows comparisons of the radial number density profiles, tangential velocity, and 3D velocity dispersion profiles of the *insitu* GCs with metallicities [Fe/H] < -1 (blue) and [Fe/H] < -1 (green). The lines show the median profiles of bootstrap samples

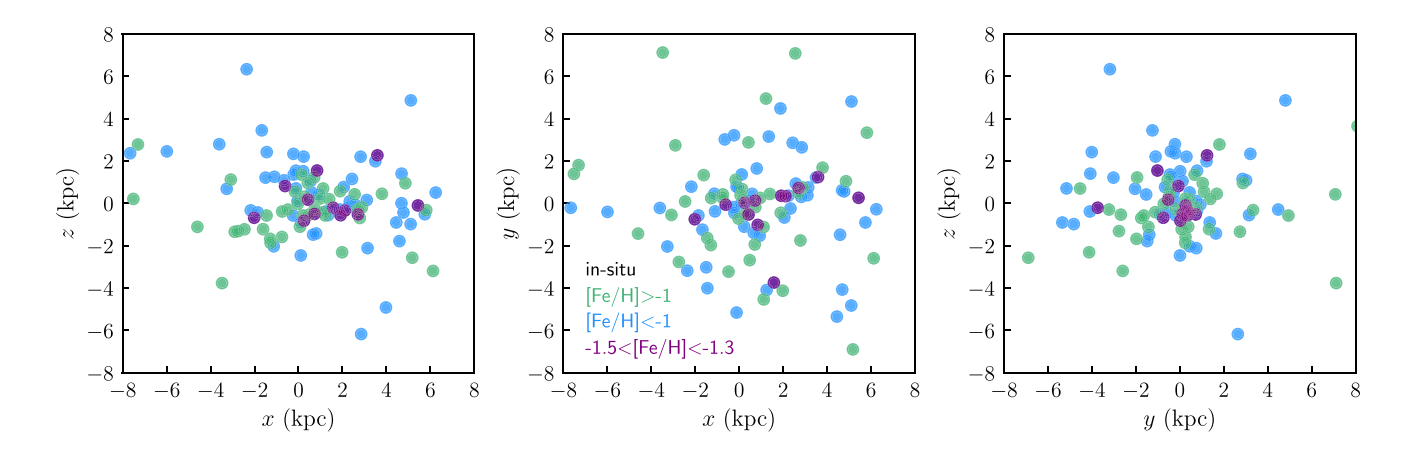


Figure 8. Projections of the spatial distribution of GCs classified as *in-situ* in different ranges of metallicity: *blue points* show clusters with [Fe/H] < -1, of these clusters in the metallicity range of the first peak in the metallicity distribution, -1.5 < [Fe/H] < -1.3, shown by *points of purple colour*, *green points* show GCs with [Fe/H] > -1. The figure shows that the distribution of high-metallicity *in-situ* GCs is more flattened around the z = 0 plane than the distribution of low-metallicity clusters. It also shows that 11 GCs in the metallicity range -1.5 < [Fe/H] < -1.3 are distributed in a rather narrow filament or prolate ellipsoid with a small c/a axes ratio.

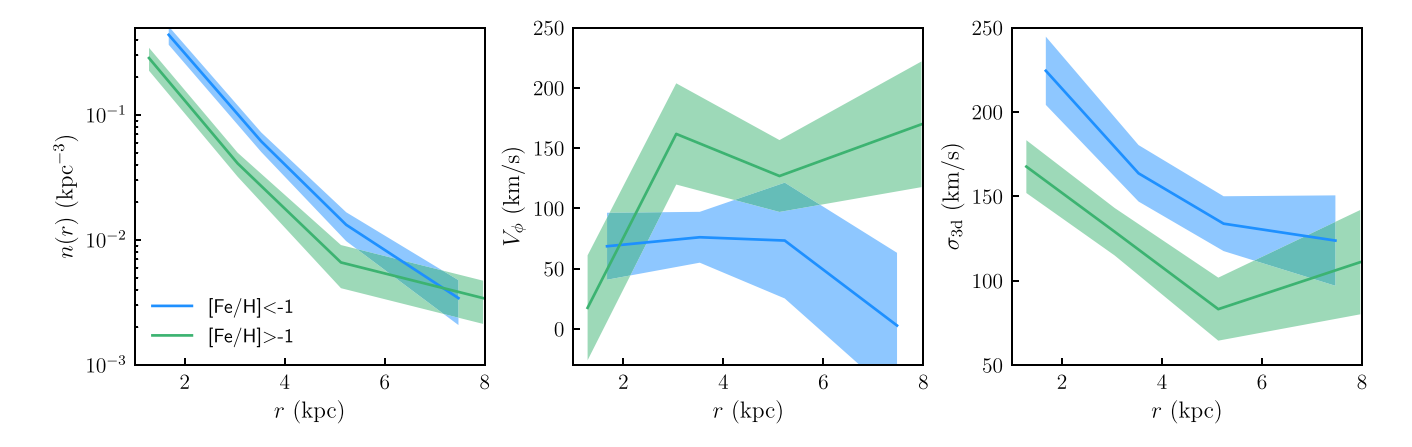


Figure 9. Profiles of number density (left panel), median tangential velocity (middle panel) and 3D velocity dispersion (right panels) of the *in-situ* GCs with metallicities [Fe/H] < -1 (blue) and [Fe/H] < -1 (green). The lines show the median profiles of bootstrap samples while shaded regions show standard deviation of the median profiles of the bootstrap samples. The left panel shows that radial distribution of the high-metallicity *in-situ* clusters is more concentrated, while the right panel shows that velocity dispersion of the high-metallicity GCs is considerably lower than that of the low-metallicity *in-situ* clusters. The middle panel shows that high-metallicity *in-situ* GCs population exhibits coherent rotation with  $V_{\phi}(r)$  reminiscent of a rotation curve, while low metallicity *in-situ* GCs also show coherent net rotation with a much smaller value of  $\approx 50 \text{ km s}^{-1}$ .

while shaded regions show the standard deviation of the median profiles of the bootstrap samples.

The figure shows that the radial distribution of the high-metallicity *in-situ* clusters is more concentrated, while their velocity dispersion is considerably lower than that of the low-metallicity *in-situ* clusters. This is because higher metallicity clusters formed within a relatively compact MW disc, while [Fe/H] < -1 clusters formed during chaotic pre-disc stages of evolution and were likely dynamically heated both by mergers and by feedback-driven inflows and outflows. As we noted above, they were also likely affected by the Milky Way bar which induced a small net  $V_{\phi} \approx 50\,\mathrm{km~s^{-1}}$  velocity (see Dillamore et al. 2023a).

Likewise, the  $V_{\phi}(r)$  profile comparisons in the middle panel shows that high-metallicity *in-situ* GCs population exhibits coherent rotation with  $V_{\phi}(r)$  reminiscent of a rotation curve, while low metallicity *in-situ* GCs also show coherent net rotation but with a

much smaller value of  $\approx$ 50 km s<sup>-1</sup>, in agreement with the change of  $V_{\phi}$  as a function of [Fe/H] in Fig. 5.

## 5 DISCUSSION

### 5.1 Comparison with previous classifications

As noted in Section 1, a number of previous studies devised methods to classify accreted and *in-situ* GCs using properties of GCs. The study most relevant for comparison with our classification method is Massari, Koppelman & Helmi (2019) because it uses similar cluster properties for classification and we thus focus on the comparison with their classification here.

All of the GCs we classify as accreted (58 in total) are also classified as accreted by Massari, Koppelman & Helmi (2019). However, their study classifies only 61 GCs (or  $\approx$  40 per cent of their sample) among our *in-situ* sample as *in-situ*. The rest are classified

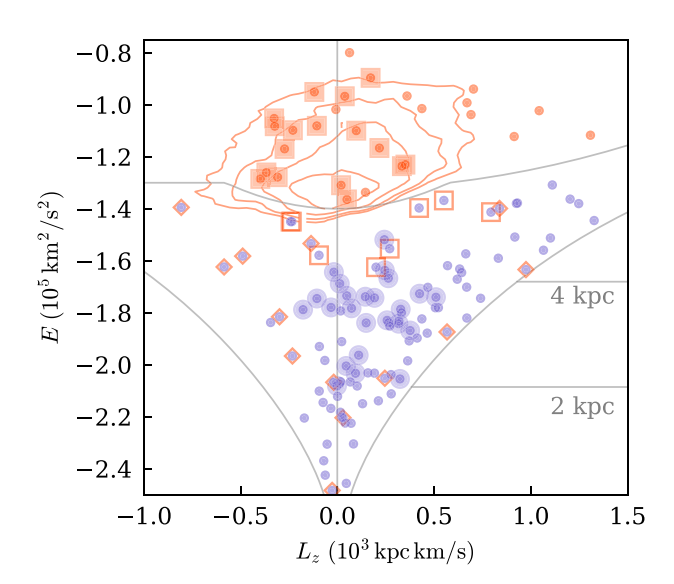


**Figure 10.** Zoom-in on the low-E portion of the  $E-L_z$  plane. Small blue (orange) filled circles mark the locations of *in-situ* (accreted) GCs according to our classification. Filled (empty) squares are accreted (*in-situ*) clusters assigned to the GS/E merger by Massari, Koppelman & Helmi (2019). Large filled circles mark those GCs that are classified as *in-situ* in our method but as the 'low-energy group' by Massari, Koppelman & Helmi (2019). Diamonds are *in-situ* clusters without a well-defined classification in Massari, Koppelman & Helmi (2019). Grey curves give maximal  $L_z$  at a given E. Orange contours give the location of the GS/E tidal debris isolated in the *Gaia* DR3 data by Belokurov et al. (2023). For comparison, horizontal grey lines mark energy levels of the circular orbits at 2 and 4 kpc.

as accreted or undetermined. Below we focus on these low-energy objects and discuss observational clues to their origin.

Fig. 10 zooms in on the portion of the  $E-L_z$  space just below the *in-situ*/accreted decision boundary where we indicate the assignment adopted by Massari, Koppelman & Helmi (2019). Only 61 of 107 classified as *in-situ* in our method (small blue-filled circles) formed in the MW according to Massari, Koppelman & Helmi (2019): they classified 25 of these clusters as 'the disc' (M-D, following their designation) and 36 as 'the bulge' (M-B).

The other 46 in-situ clusters in our classification are classified by Massari, Koppelman & Helmi (2019) as follows. 24 clusters (large blue circles) are assigned to the 'low-energy group', which was later interpreted to be a signature of an accretion event at  $z \sim$ 1, sometimes referred to as Kraken (Kruijssen et al. 2019b, 2020) or Koala (Forbes 2020). Note that the latter two works show good agreement with the classification presented in Massari, Koppelman & Helmi (2019) but unfortunately cannot be considered as independent lines of evidence as both base their analysis on the GC group assignment of Massari, Koppelman & Helmi (2019) to begin with. Note that Horta et al. (2021) present chemo-dynamical evidence for the debris of an ancient massive accretion event they call Heracles based on the APOGEE data, however the direct connection between Kraken/Koala and Heracles has not been established. There are also 8 GCs assigned by Massari, Koppelman & Helmi (2019) to the GS/E merger, but classified as in-situ in our scheme; these are marked with empty orange squares. Finally, there are 14 GCs with undetermined classification in Massari, Koppelman & Helmi (2019), marked with orange diamonds: these either have '?' or 'XXX' for the possible progenitor or were not included in their catalogue (7 out of 14).

To gain a better perspective on the chemo-dynamic properties of these various GC groups, Fig. 11 shows cluster orbital eccentricity (computed with the pericentre and apocentre estimates from the H. Baumgardt database, see Section 2) as a function of metallicity in the left panel, eccentricity as a function of  $L_{\perp} = \sqrt{L_x^2 + L_y^2}$  – the component of the angular momentum perpendicular to  $L_z$  - in the middle panel, and the distribution of the GCs (where abundance measurement is available) in the plane of [Mg/Fe] and [Al/Fe] in the right panel. Here we have included several literature values that were corrected to the APOGEE abundance scale, as described in Appendix A. The GCs with non-APOGEE measurements of [Al/Fe] and [Mg/Fe] from the literature include NGC 1261 (Marino et al. 2021), Rup 106 (Brown, Wallerstein & Zucker 1997), NGC 4833 (Carretta et al. 2014), NGC 5286 (Marino et al. 2015), NGC 5466 (Lamb et al. 2015), NGC 5927 (Mura-Guzmán et al. 2018), NGC 5986 (Johnson et al. 2017c), NGC 6139 (Bragaglia et al. 2015), NGC 6229 (Johnson et al. 2017a), NGC 6266 (Lapenna et al. 2015), NGC 6355 (Souza et al. 2023), NGC 6362 (Massari et al. 2017), NGC 6402 (Johnson et al. 2019), NGC 6440 (Origlia, Valenti & Rich 2008), NGC 6522 (Ness, Asplund & Casey 2014), NGC 6528 (Muñoz et al. 2018), NGC 6584 (O'Malley & Chaboyer 2018), NGC 6624 (Valenti, Origlia & Rich 2011), NGC 6864 (Kacharov, Koch & McWilliam 2013), and NGC 6934 (Marino et al. 2021).

Recently, we showed that *in-situ* and accreted GCs separate well in the space of [Mg/Fe]-[Al/Fe] (Belokurov & Kravtsov 2023). In addition, at [Fe/H] > -2 the *in-situ* stars have higher values of [Mg/Fe] compared to those accreted (Belokurov & Kravtsov 2022). This trend, however, is blurred by the internal GC evolution where Mg can be destroyed to make Al. As a result, clusters may end up having lower values of [Mg/Fe]. Nevertheless, the anomalous chemistry is betrayed by their elevated [Al/Fe] ratio. Thus, in the plane of [Mg/Fe]-[Al/Fe] GCs can move diagonally from top left to bottom right, as indicated by the black dashed line. While the chemical plane of [Al/Fe] and [Mg/Fe] appears to work well to separate the GCs into two distinct groups, it would be beneficial to explore the use of elemental abundances not affected by the cluster's secular evolution. In connection to this, most recently, other chemical tags have been proposed to pin down the origin of the Galactic GCs. For example, Minelli et al. (2021) advocate the use of Sc, V, and Zn for metallicity [Fe/H] > -1, while Monty et al. (2023, in preparation) show that Eu can be used as a strong tag of the GS/E GCs. We note that recently there have been other attempts to isolate chemical differences between pre-classified in-situ and accreted MW GCs (see e.g. Horta et al. 2020).

Only two GCs classified as GS/E in our scheme (NGC 288 and NGC 5286) lie in the top right corner of the [Mg/Fe]–[Al/Fe] plane shown in the right panel of Fig. 11. For both of these clusters recent chemical abundance measurements indicate that these clusters are probably not associated with the GS/E merger (see Monty et al. 2023). There is an additional cluster, NGC 6584, which lacks a clear progenitor but is deemed to be accreted (Massari, Koppelman & Helmi 2019; Forbes 2020); it is classified as accreted in our scheme.

Four GCs classified as *in-situ* in our scheme using the  $E-L_z$  boundary lie in the bottom left corner of the [Mg/Fe]–[Al/Fe] plane dominated by accreted clusters (although three are close to the nominal boundary). Assuming all four are indeed misclassified and were accreted, the fraction of accreted clusters among GCs classified as *in-situ* by our scheme can be classified as  $\approx 4/39 \approx 10$  per cent, where 39 is the number of *in-situ* GCs above the dashed line in the [Mg/Fe]–[Al/Fe] plane.

Focusing on the 'low-energy group' of globular clusters (large blue circles), it is difficult to see how these objects can be a part of

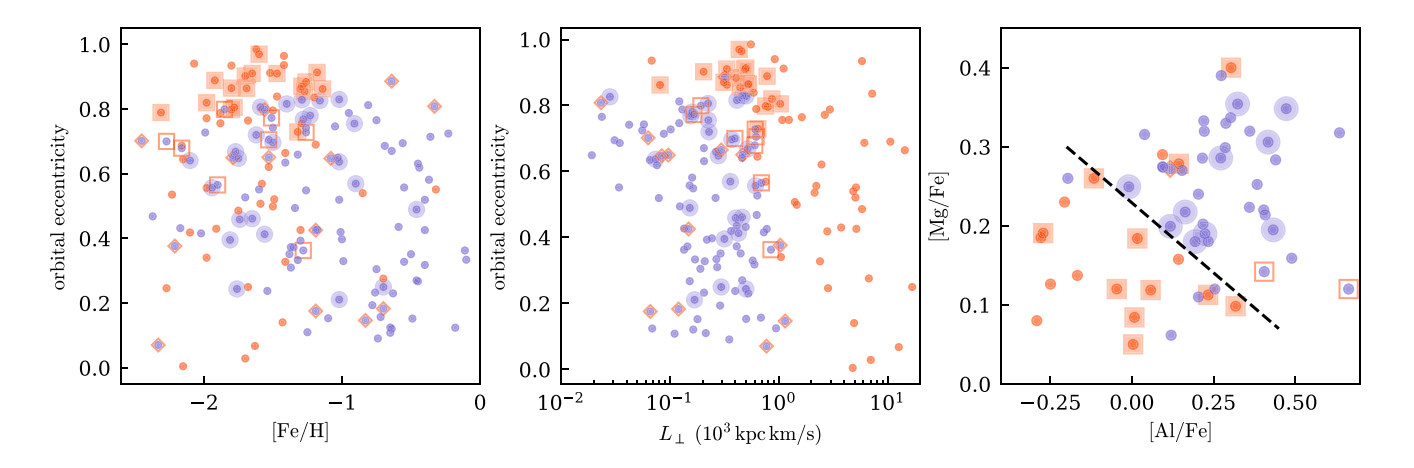


Figure 11. Orbital and chemical properties of *in-situ* and accreted GCs. Left: Orbital eccentricity as a function of metallicity. Middle: Eccentricity as a function of  $L_{\perp}$  component of the angular momentum. Right: [Mg/Fe] vs [Al/Fe] for GCs with available abundance measurements (see Appendix A for comparison between APOGEE and literature values). Small blue/purple (red/orange) filled circles mark the locations of *in-situ* (accreted) GCs according to our classification. Filled (empty) squares are accreted (*in-situ*) clusters assigned to the GS/E merger by Massari, Koppelman & Helmi (2019). Large filled circles mark those GCs that are classified as *in-situ* in our method but as the 'low-energy group' by Massari, Koppelman & Helmi (2019). Diamonds are *in-situ* clusters without a well-defined classification in Massari, Koppelman & Helmi (2019).

a single accretion event. These 24 GCs do not cluster together in any of the orbital properties considered. Instead, they span a large range of E,  $L_z$ ,  $L_\perp$ , and eccentricity. This is in stark contrast with the GS/E highlighted with filled orange squares: these GCs have a narrow range of eccentricity and  $L_\perp$ . In terms of  $L_z$ , the low-energy group GCs appear to have an extent similar to the GS/E members. This, however, is an illusion: the available range of  $L_z$  is a strong function of energy and drops with decreasing E. For the energy level of the clusters labelled as the 'low-energy group', the  $L_z$  range is less than half of that at the level of the GS/E GCs. Therefore, the relative  $L_z$  dispersion of these GCs is larger by more than a factor of 2. These clusters also have a clear net prograde motion with a mean  $V_\phi \approx 60 \, \mathrm{km \ s^{-1}}$  similar to the bulk of the *in-situ* GCs and typical of the Aurora population.

In terms of their chemistry, all 10 (out of 24) of the 'low-energy group' GCs with available abundance measurements lie with the rest of the *in-situ* clusters in the [Mg/Fe]–[Al/Fe] plane shown in the right panel of Fig. 11. We conclude that there is no strong evidence in favour of a distinct low-energy group of clusters because in every property considered, these clusters span the range typical of *in-situ* GCs.

Note that the main reason these clusters were classified as accreted by Massari, Koppelman & Helmi (2019) is because they are located outside of the nominal 'bulge' radius of 3.5 kpc. However, this adopted size is rather arbitrary because the peanut bulge of the Milky Way has a radial extent of  $\approx 1.5$  kpc, while at larger distances stellar distribution is arranged into a prominent bar (see e.g. fig. 1 in Wegg, Gerhard & Portail 2015; Barbuy, Chiappini & Gerhard 2018a). Incidentally, in our catalogue, 14 out of the 24 GCs assigned to the low-energy group by Massari, Koppelman & Helmi (2019) have Galactocentric distances smaller than 3.5 kpc (also see Fig. 10).

Let us now briefly consider the 8 GCs (highlighted with open orange squares) classified as *in-situ* in our scheme, but associated with the GS/E event by Massari, Koppelman & Helmi (2019). First, we note that none of these GCs are assigned to GS/E in either the original study of Myeong et al. (2018) or the expanded analysis of Myeong et al. (2019). On the other hand, we classify as accreted all clusters assigned to GS/E by Myeong et al. (2018) and 18 (of 21) in

Myeong et al. (2019). Similarly, all 19 GCs classified by Limberg et al. (2022) as belonging to GS/E are deemed accreted here. As Fig. 10 illustrates, the density of the GS/E stellar component drops abruptly below  $E=-1.4\times10^5~\rm km^2~s^{-2}$ . Most of the eight alleged by Massari, Koppelman & Helmi (2019) GS/E GCs lie outside of the orange contours and thus have values of total energy lower than the bulk of the GS/E's tidal debris.

Another concern is that five out of eight GCs have positive  $L_z$ . As discussed in Belokurov et al. (2023), the GS/E debris cloud has an apparent tilt in the E,  $L_z$  space such that the higher energy stars show net prograde motion. The net prograde motion of the eight suggested low-energy GCs is counter to this trend. While the highenergy GS/E GCs all have high orbital eccentricity, i.e. 0.8 < e < 1, the additional low-energy candidate objects have significantly lower and more varied eccentricities, i.e. 0.3 < e < 0.8. Unfortunately, we have chemical information only for two out of eight clusters and these particular objects are both consistent with being a part of the *in-situ* population.

Finally, nothing makes the 14 GCs with uncertain progenitor (marked with orange diamonds) stand out from the rest of the *in-situ* clusters. These span a very broad range of E,  $L_z$ , and  $L_\perp$ . Chemical information is available for only one object from this group and it places it in the *in-situ* dominated region.

Malhan et al. (2022) presented classification of the Milky Way's GCs and streams using estimates of their total energy and actions using Gaia EDR3 kinematic measurements. All but one of the accreted structures these authors identify lie above the *in-situ*/accreted boundary we use and thus would also be classified as accreted by our method. One of their identified systems, Pontus, lies just below our classification boundary in the *in-situ* region. We note, however, that as shown by Dillamore et al. (2022) dynamical effects of the Milky Way bar can create horizontal clustering of stars and other dynamical traces in the general vicinity of the  $E-L_z$  region where Pontus is identified. It remains to be seen whether chemical abundances of this system are consistent with its accreted or *in-situ* origin.

Sun et al. (2023) presented a classification scheme for *in-situ* and accreted GCs that largely follows the approach of Massari, Koppelman & Helmi (2019). In particular, similarly to Massari,

Koppelman & Helmi (2019) these authors identify the in-situ GCs using 'disc' and 'bulge' populations but defined using a different set of criteria involving spatial and kinematic properties from the Gaia DR3 measurements by Baumgardt & Vasiliev (2021). These criteria identify 45.3 per cent GCs as formed in-situ and 38.4 per cent as accreted, with the remaining 16.3 per cent were deemed to have uncertain origin. Thus, although the approach is similar to Massari, Koppelman & Helmi (2019) different criteria used to identify *in-situ* clusters resulted in a higher in-situ GC fraction. Callingham et al. (2022) build a multicomponent model of Galactic GCs – similar to a Gaussian Mixture - in the space of integrals of motion, metallicity and age. This is currently the only truly unsupervised attempt in the literature aimed at creating an objective and unbiased clustering scheme for the Galactic GCs. While in principle this method can be used to create GC groups in a fully automated fashion, as the authors acknowledge, in practice there is a substantial overlap between lowenergy GCs. As a result, Callingham et al. (2022) are forced to initialise their groups with classifications from the literature (e.g. Massari, Koppelman & Helmi 2019). Even with the addition of this prior, separating low-energy GCs is hard and Callingham et al. (2022) end up with an overmassive 'Kraken' group which appears to violate the MW stellar halo mass constraint (see e.g. Deason, Belokurov & Sanders 2019; Mackereth & Bovy 2020). The biggest difference between the Sun et al. (2023), Callingham et al. (2022), and our classifications is in that the former assign 'Kraken' lowenergy clusters to the accreted component. As we discussed above, however, there is no clear evidence that these clusters are a distinct grouping that can be clearly associated with an accretion event.

# 5.2 Comparison with models and implications for GC formation

While detailed comparisons with models of GC formation are beyond the scope of this study, here we will discuss general comparisons focusing on the fraction of accreted clusters estimated in our classification and in the models. We will also present comparisons with statistics of the *in-situ* and accreted stellar particles in the FIRE-2 simulations of the MW-sized haloes (Hopkins et al. 2018a; Wetzel et al. 2023) and discuss the implications of these comparisons for models of GC formation and evolution.

As we noted above,  $\approx 1/3$  of surviving GCs in our classification are accreted. This is lower than in some of the recent models of GC formation. For example, the model of Chen & Gnedin (2022) predicts for MW-sized hosts the ratio of the number of accreted to *in-situ surviving* GCs of  $\sim 2/1$  to 3/1. The number of *in-situ* GCs that form in the MW progenitor in their model is actually larger than the number of accreted clusters that ever formed, but many more *in-situ* clusters get tidally disrupted compared to the accreted clusters and the number of surviving clusters is thus dominated by the accreted GCs. The results of the model are thus quite sensitive to how tidal disruption of clusters is modelled. For example, in the previous version of this model (see Fig. 6 in Choksi & Gnedin 2019) with a different disruption model predicted population of the surviving GCs was dominated by the *in-situ* clusters.

E-MOSAIC GC formation model predicts that the mean  $52 \pm 1$  per cent of the surviving GCs were born in-situ (Keller et al. 2020), although further analyses showed that the *ex situ* fractions vary non-negligibly from object to object and have a range of  $\approx 37 \pm 11$  per cent which is similar to the fraction in our classification (Kruijssen et al. 2019a; Trujillo-Gomez et al. 2021). Trujillo-Gomez et al. (2023), on the other hand, find median accreted fraction of  $\approx 60$  per cent in the same E-MOSAIC model, but with substantial

scatter around it; the different fractions in different E-MOSAIC analyses are due to different selection of GC samples indicating sensitivity of the accreted fraction to details of selection. Generally, the accreted fraction is expected to have a significant scatter due to different assembly histories of objects of the same halo mass. Their model also predicts that the fraction of surviving clusters is approximately the same among accreted and *in-situ* clusters. We thus see a significant variation among GC models in what they predict for the accreted and *in-situ* GC populations and their survival.

Overall, galaxy formation models predict that the accreted fraction of stellar population is very small in galaxies of  $M_{\star} \lesssim 10^{10} \, \rm M_{\odot}$  but increases rapidly for larger masses reaching accreted fractions of  $\approx 20$ –50 per cent for galaxies with  $M_{\star} \approx 10^{11} \, \rm M_{\odot}$  (e.g. Qu et al. 2017; Clauwens et al. 2018; Pillepich et al. 2018; Davison et al. 2020). However, these fractions refer to the total masses of accreted and *in-situ* populations at all radii.

As we saw, our classification implies that GC population within galactocentric distance of 10 kpc is dominated by *in-situ* clusters. We estimated the mass fraction of accreted stellar particles within such galactocentric distance in the seven MW-sized objects from the FIRE-2 simulation suite (Hopkins et al. 2018a; Wetzel et al. 2023) and find that  $f_{\rm acc}(<10\,{\rm kpc})=m_{\star,{\rm acc}}/m_{\star,{\rm tot}}$  ranges from 2 to 7 per cent in 5 out of 7 galaxies, and reaches 13 per cent and 25 per cent in the other two systems. Overall, therefore, simulations predict that stellar population of MW-sized galaxies within the central 10 kpc is dominated by the *in-situ* stars.

We have carried out another comparison, which is aimed to be more directly related to the accreted fraction of GCs. Namely, we examined distributions of several properties of stellar particles in the FIRE-2 simulations of the MW-sized galaxies m12b, m12c, m12f, m12i, m12m, m12r, and m12w but weighted or selected so as to match metallicity distributions of the *in-situ* and accreted MW GCs. Fig. 12 shows a comparison of the radial number density profiles of *in-situ* and accreted stellar particles in the FIRE-2 objects weighted in this way to the number density profiles of the *in-situ* and accreted GCs in our classification. The density profiles of stellar particles constructed this way are normalized so that the number density profile of the *in-situ* particles approximately matches the number density profile of *in-situ* in amplitude. The same normalization factor is used for both the *in-situ* and accreted stellar particles.

Fig.12 shows that the number density profiles of *in-situ* and accreted stellar particles match the relative amplitude and shapes of the corresponding density profiles of the MW GCs quite well. The match is especially good for three objects – m12f, m12r, m12b – that have *in-situ* age-[Fe/H] stellar sequences closest to the corresponding sequence of *in-situ* GCs (see fig. 13 in Belokurov & Kravtsov 2023). The *in-situ* star particles are more centrally concentrated, while accreted particles have a much more extended distribution. This is generally found in models of GC evolution (Chen & Gnedin 2022; Reina-Campos et al. 2022a), but here we see a remarkable match of both shapes and relative amplitudes of the observed profiles.

Fig.13 shows comparisons of the number density, median tangential velocity  $V_{\phi}$ , and 3D velocity dispersion  $\sigma_{3d}$  profiles of *insitu* stellar particles with [Fe/H] < -1 and [Fe/H] > -1 with the corresponding profiles of the *in-situ* MW GCs. The metallicity trend in the number density profile is reproduced quite well. The metallicity trend in the  $V_{\phi}$  profile is also qualitatively reproduced.

The match of the relative amplitude and shape of the GC number density profiles of *in-situ* and accreted GCs by the stellar particle number density profiles in Fig. 12 indicates that simulations capture

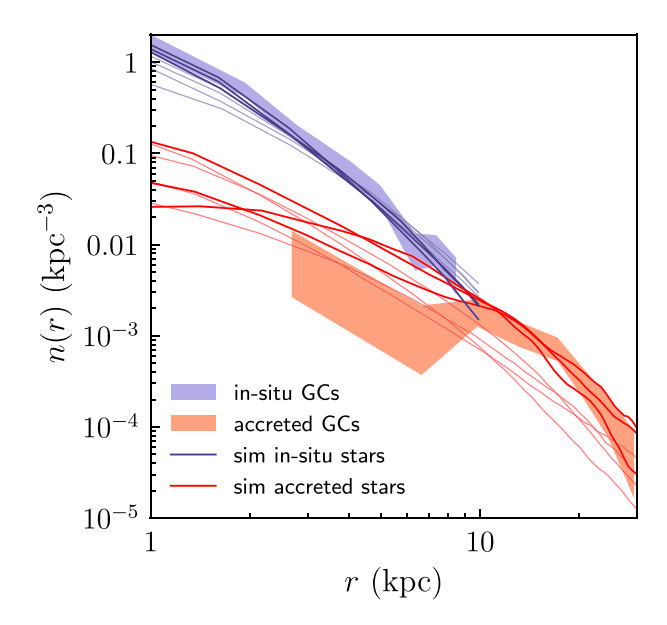


**Figure 12.** Number density of *in-situ* (blue) and accreted (red) GCs as a function of their galactocentric distance *r*. The shaded regions show the scatter around median profiles in the bootstrap samples of the MW GCs, while the blue and red lines show the number density of stellar particles from the FIRE-2 simulations of the MW-sized hosts (namely, objects m12f, m12i, m12m, m12w, m12r, m12b, m12c). The *in-situ* and accreted stellar particles are weighted such that their metallicity distribution matches that of the *in-situ* and accreted MW GCs, as described in the text. The three objects, m12f, m12r, m12b, that are closest in age—metallicity relation to the MW GCs (see fig. 13 in Belokurov & Kravtsov 2023) are shown by the stronger lines, while the other objects are shown by the thinner lines.

realistically formation of stars and their dynamics. Assuming this is the case, the match *implies that GC formation is a part of regular star formation in the MW progenitor*. However, given that the metallicity distribution of GCs is different from that of the MW *in-situ* stars, GC formation was confined only to certain periods of the Galaxy evolution. These periods likely reflected periods of high gas accretion

either when MW progenitor halo was still in the fast accretion regime or during spikes in the gas accretion rate in the slow accretion regime. One of such spikes could have been associated with the GS/E merger  $\approx 10$  Gyr ago. This merger proceeded for a while and could have affected formation of stars and GCs with metallicities between [Fe/H]  $\approx -1.5$  and -0.5.

The good match of the observed GC and simulated stellar number density profiles also implies that disruption of GCs should not have a strong distance dependence, otherwise radial distribution of GCs would be different than the radial stellar particles that are not subject to disruption. This is in general agreement with models of GC formation and evolution (Keller et al. 2020; Gieles & Gnedin 2023). Likewise, the agreement of the *in-situ* number density profiles at different metallicities indicates that tidal disruption should not have a strong metallicity dependence, which agrees with the model results of (see fig. 15 of Keller et al. 2020, and O. Gnedin private communication).

Recently, there has been a number of efforts to include explicitly the formation and evolution of massive gas clumps in high-resolution hydro-dynamical simulations of the Milky Way disc. For example, Clarke et al. (2019) show that  $\sim\!100$  of well-resolved gas clumps with masses between  $3\times10^7$  and  $10^{10}M_{\odot}$  can form in the early Milky Way. Most massive of these can sustain prolonged star formation and migrate through the inner regions of the Galaxy leaving a distinct imprint on the disc's chemical, structural and kinematic behaviour (see also Beraldo e Silva et al. 2020; Debattista et al. 2023; Garver et al. 2023). The massive, early formed gas clumps described in the above models appear to be a natural progenitor of the population of Galactic disc's globular clusters discussed here.

It is interesting to note that mass of the stellar halo of our Galaxy is only  $1.4 \pm 0.4 \times 10^9 \, M_\odot$  (Deason, Belokurov & Sanders 2019), while *in-situ* stellar mass of our galaxy is  $\approx 6 \times 10^{10} \, M_\odot$  (e.g. Licquia & Newman 2015). The overall fraction of accreted stars in our Galaxy is thus  $f_{\rm acc} \approx 2$  per cent, while the fraction of accreted GCs in our classification by number is much larger:  $58/107 \approx 54$  per cent. By mass, the mass fraction in surviving accreted GCs is  $\approx 40$  per cent, although if we estimate the mass fraction of accreted clusters using the initial GCs masses in the *in-situ* and accreted clusters estimated by Baumgardt & Makino

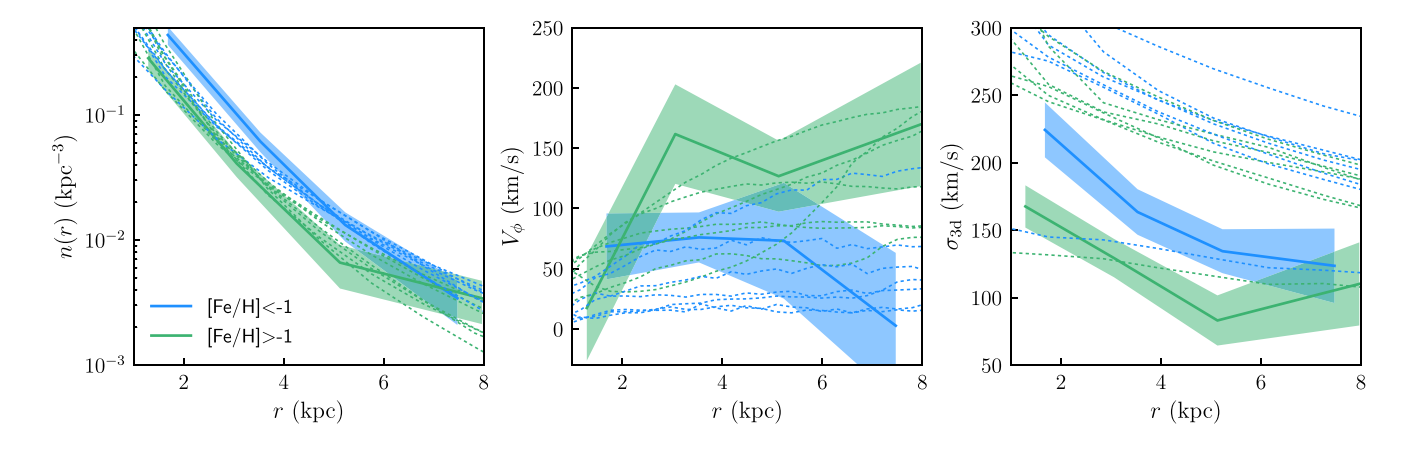


Figure 13. The radial profiles of the *in-situ* MW GCs of low ([Fe/H] < -1) and high ([Fe/H] > -1) metallicity shown in Fig. 9 above compared with the corresponding profiles of *in-situ* stellar particles from the FIRE-2 simulations of the MW-sized galaxies of the same metallicity ranges. In computing these *in-situ* stellar particles are weighted such that their metallicity distribution matches that of the *in-situ* MW GCs, as described in the text. The figure shows that the *in-situ* stellar particles in simulations match the radial density profile and profile of the tangential velocity, as well as their changes between low- and high-metallicity samples. The trend is also reproduced for the velocity dispersion, but velocity dispersions in simulations are generally considerably higher than for MW GCs, except for the dispersion in the object m12r.

(2003) the initial accreted mass fraction is  $\approx 20\,$  per cent. Regardless of how we estimate the accreted fraction, it is at least ten times larger than the overall accreted mass fraction in the MW's stellar population.

It is likely that this is due to a combination of factors. First, MW stopped forming *in-situ* GCs  $\gtrsim 10$  Gyr ago (see ages in Fig. 3), while it continued to accrete GCs and form *in-situ* stars. Secondly, the number of GCs scales almost linearly with halo mass over more than five orders of magnitude in galaxy stellar mass with  $\eta_{\rm GC} = M_{\rm GCs}/M_{\rm h} \approx 3 \times 10^{-5}$  (see Spitler & Forbes 2009; Hudson, Harris & Harris 2014; Harris, Blakeslee & Harris 2017; Forbes et al. 2018; Dornan & Harris 2023), although it is somewhat uncertain at the smallest masses and may deviate from linearity in that regime (Bastian et al. 2020; De Lucia et al. 2023). Galaxy stellar mass scales, on the other hand, scales non-linearly in the dwarf galaxy regime (e.g. Nadler et al. 2020). Thus, dwarf galaxies bring proportionally more GCs compared to stars when they merge with the MW.

#### 5.3 Caveats

As we noted before, the use of a categorical boundary almost certainly will misclassify some accreted objects with energies below the boundary and vice versa. This needs to be kept in mind when considering individual GCs. Eventually, as reliable chemical element ratios and orbital parameter estimates become available for more clusters, it should be possible to refine the classification presented here. For example, the  $\omega$  Centauri and NGC 6273 clusters are classified as *in-situ* clusters by our method but are likely to be remnant nuclear star clusters of accreted galaxies due to their large metallicity spread (e.g. Pfeffer et al. 2021). We mark the clusters that have some indications of being misclassified in comments in Table D1 in Appendix D.

Overall, our estimates indicate that the fraction of accreted clusters among those we classified as in-situ is likely  $\lesssim 10$  per cent (or fewer than 15 clusters). First, we do not see evidence of a significant sub-population of these clusters with distinct chemical and orbital properties. Secondly, the number density profiles of in-situ and accreted stellar particles that match the corresponding profiles of the GCs in our classification have relative amplitudes that correspond to  $\lesssim 10$  per cent of accreted stellar particles at r < 10 kpc. Third, detailed analyses of galaxy formation simulations indicate that MW's halo and disc form earlier than most objects of similar mass (Dillamore et al. 2024; McCluskey et al. 2024; Semenov et al. 2023). Dillamore et al. (2024) recently showed that such systems also have smaller than average fraction of accreted stars. Thus, it is very unlikely that the fraction of accreted GCs in the MW is high, especially in the central 10 kpc from the Galaxy centre.

## 6 SUMMARY AND CONCLUSIONS

We use the [Al/Fe]-calibrated *in-situ*/accreted classification in the  $E-L_z$  plane introduced in Belokurov & Kravtsov (2023) to demonstrate that such classification results in two GC populations with distinct spatial, kinematic and chemical abundance distributions. The specific results presented in this paper and their implications are as follows.

(i) Just under two thirds of the currently known GCs in the Galaxy are classified by us as *in-situ*. This implies that the GC accreted fraction  $\approx 35$  per cent is much lower than some previous estimates (see e.g. Massari, Koppelman & Helmi 2019; Forbes 2020) but not in strong tension with others (e.g. Malhan et al. 2022; Sun et al. 2023).

- (ii) Fig. 2 shows that our classification results in GC samples with qualitatively different spatial distributions. *In-situ* clusters are located mainly at  $\lesssim 10$  kpc from the centre of the Galaxy, while accreted clusters are mainly located at larger distances. The distribution of accreted clusters is almost spherical, while *in-situ* clusters are distributed in a flattened configuration aligned with the MW disc.
- (iii) Our classification splits the clusters into two distinct sequences in the age—metallicity plane (Fig. 3) with *in-situ* GCs tracing the evolution of metallicity as a function of time of our Galaxy.
- (iv) The accreted and *in-situ* clusters have different distributions of metallicities (Fig. 4). Most accreted clusters have [Fe/H]  $\lesssim -1$  and distribution of metallicities has a single peak at [Fe/H]  $\approx -1.6$ . Metallicity distribution of the *in-situ* clusters spans a much wider range of [ -2.3, 0] and has two peaks centered at [Fe/H]  $\approx -1.4$  and [Fe/H]  $\approx -0.7$ . The weak bi-modality of the overall metallicity distribution of the MW GCs is thus entirely due to the *in-situ* clusters.
- (v) We show that the *in-situ* GCs in our classification show a clear disc spin-up signature the increase of median  $V_{\phi}$  at metallicities [Fe/H]  $\approx -1.3 \div -1$  similar to the signature exhibited by the *in-situ* stars of the Milky Way.
- (vi) This feature signals MW's disc formation and the fact that it is also present in the kinematics of the *in-situ* GCs means that most GCs with metallicities of  $[Fe/H] \gtrsim -1.3$  were born in the Milky Way disc, while lower metallicity GCs were born during early, turbulent, pre-disc stages of the evolution of the Galaxy and are part of the Aurora stellar component of the Milky Way.
- (vii) Ages and metallicities of *in-situ* GCs and the spin-up metallicity range indicate that MW's disc formed  $\approx$ 11.7–12.7 Gyr ago or at  $z \approx 3.1-5.3$ .
- (viii) We explicitly show radial and velocity distributions of the Aurora clusters and higher metallicity *in-situ* clusters are different (Section 4.5 and Fig. 9).
- (ix) We show that the accreted and *in-situ* GCs are well separated in the plane of [Al/Fe] [Mg/Fe] abundance ratios.
- (x) We show that the radial distribution of the *in-situ* and accreted GCs is very similar to the radial distribution of the *in-situ* and accreted stellar particles in the FIRE-2 galaxy formation simulations if particles are selected to have metallicity distribution similar to that of the MW GCs. This indicates that MW globular clusters are born as part of the normal star formation in the MW progenitor but during epochs most conducive for their formation.

The classification method presented in this paper is meant to be applicable broadly to the entire GC population of the Milky Way. It is based only on the total energy and  $L_{\tau}$  angular momentum because these are some of the very few quantities that are available for the entire GC sample. It is clear thus that the method is unlikely to be 100 per cent accurate. Nevertheless, we estimate that not more than  $\approx 10$  per cent of the clusters classified as *in-situ* in our method may actually be accreted. This classification can of course be refined further using additional formation for individual clusters, such as [Al/Fe] and [Mg/Fe] abundance ratios, as it becomes available. For example,  $\omega$  Centauri and NGC 6273 clusters are likely misclassified by our method as in-situ, given the evidence for large metallicity spread in these systems which implies that they have likely been nuclear star clusters in accreted galaxies (e.g. Pfeffer et al. 2021). We indicate GCs that may be misclassified by our method in the comments column of Table D1, in which our classification for individual clusters is presented.

The presented classification should be useful for testing models of globular cluster formation in the cosmological context. We stress, however, that recent analyses of galaxy formation simulations in comparisons with the kinematics of the *in-situ* stars of the Milky Way indicate that MW's halo and disc form earlier than most objects of similar mass (Belokurov & Kravtsov 2022; Dillamore et al. 2024; McCluskey et al. 2024; Semenov et al. 2023). Dillamore et al. (2024) recently showed that galaxies that undergo a GS/E-like merger and which form disc as early as the Milky Way have much smaller than average fractions of accreted stars. Thus, care should be taken when comparing models with specific MW GC sample and its accreted and *in-situ* subpopulations.

#### **ACKNOWLEDGEMENTS**

We are grateful to Holger Baumgardt and Oleg Gnedin for useful discussions and to Eugene Vasiliev, Davide Massari, Marta Reina-Campos, Stephanie Monty for their comments that helped improve the quality of this manuscript. AK was supported by the National Science Foundation grants AST-1714658 and AST-1911111 and NASA ATP grant 80NSSC20K0512. VB acknowledges support from the Leverhulme Research Project Grant RPG-2021-205: 'The Faint Universe Made Visible with Machine Learning'. This research made use of data from the European Space Agency mission Gaia (http://www.cosmos.esa.int/gaia), processed by the Gaia Data Processing and Analysis Consortium (DPAC; http://www.cosmos.esa.int/web/gaia/dpac/consortium). Funding for the DPAC has been provided by national institutions, in particular the institutions participating in the Gaia Multilateral Agreement.

This paper made used of the Whole Sky Database (wsdb) created by Sergey Koposov and maintained at the Institute of Astronomy, Cambridge with financial support from the Science & Technology Facilities Council (STFC) and the European Research Council (ERC). We also used FIRE-2 simulation public data (Wetzel et al. 2023, http://flathub.flatironinstitute.org/fire), which are part of the Feedback In Realistic Environments (FIRE) project, generated using the GIZMO code (Hopkins 2015) and the FIRE-2 physics model (Hopkins et al. 2018b). Analyses presented in this paper were greatly aided by the following free software packages: NUMPY (Oliphant 2015), SCIPY (Jones et al. 01), MATPLOTLIB (Hunter 2007), and SCIKITLEARN (Pedregosa et al. 2011). We have also used the Astrophysics Data Service (ADS) and arXiv preprint repository extensively during this project and the writing of the paper.

#### DATA AVAILABILITY

This study uses allStarLite-dr17-synspec\_rev1 and apogee\_astroNN-DR17 catalogues publicly available at https://www.sdss.org/dr17/irspec/spectro\_data/. The catalogue of the MW globular clusters with distances used in this study is publicly available at https://people.smp.uq.edu.au/HolgerBaumgardt/globula r/. The FIRE-2 simulations used in this study are available at http://flathub.flatironinstitute.org/fire.

#### REFERENCES

Adamo A. et al., 2020, Space Sci. Rev., 216, 69
 Ankerst M., Breunig M. M., Kriegel H.-P., Sander J., 1999, ACM SIGMOD Record, 28, 49http://doi.acm.org/10.1145/304181.304187

Armandroff T. E., 1989, AJ, 97, 375

Ashman K. M., Zepf S. E., 1992, ApJ, 384, 50

Ashman K. M., Zepf S. E., 2001, AJ, 122, 1888

Barbuy B. et al., 2016, A&A, 591, A53

Barbuy B., Chiappini C., Gerhard O., 2018a, ARA&A, 56, 223

Barbuy B. et al., 2018b, A&A, 619, A178

```
Bastian N., Pfeffer J., Kruijssen J. M. D., Crain R. A., Trujillo-Gomez S., Reina-Campos M., 2020, MNRAS, 498, 1050
```

Baumgardt H., 2017, MNRAS, 464, 2174

Baumgardt H., Hilker M., 2018, MNRAS, 478, 1520

Baumgardt H., Makino J., 2003, MNRAS, 340, 227

Baumgardt H., Vasiliev E., 2021, MNRAS, 505, 5957

Baumgardt H., Sollima A., Hilker M., 2020, PASA, 37, e046

Baumgardt H., Hénault-Brunet V., Dickson N., Sollima A., 2023, MNRAS, 521, 3991

Beasley M. A., Baugh C. M., Forbes D. A., Sharples R. M., Frenk C. S., 2002, MNRAS, 333, 383

Belokurov V., Kravtsov A., 2022, MNRAS, 514, 689

Belokurov V., Kravtsov A., 2023, MNRAS, 525, 4456

Belokurov V., Erkal D., Evans N. W., Koposov S. E., Deason A. J., 2018, MNRAS, 478, 611

Belokurov V., Vasiliev E., Deason A. J., Koposov S. E., Fattahi A., Dillamore A. M., Davies E. Y., Grand R. J. J., 2023, MNRAS, 518, 6200

Beraldo e Silva L., Debattista V. P., Khachaturyants T., Nidever D., 2020, MNRAS, 492, 4716

Bland-Hawthorn J., Gerhard O., 2016, ARA&A, 54, 529

Bragaglia A., Carretta E., Sollima A., Donati P., D'Orazi V., Gratton R. G., Lucatello S., Sneden C., 2015, A&A, 583, A69

Brown J. A., Wallerstein G., Zucker D., 1997, AJ, 114, 180

Burkert A., Forbes D. A., 2020, AJ, 159, 56

Burkert A., Brown J. H., Truran J. W., 1996, in Burkert A., Hartmann D. H., Majewski S. A.eds, ASP Conf. Ser. Vol. 112, The History of the Milky Way and Its Satellite System. Astron. Soc. Pac., San Francisco, p. 121

Callingham T. M., Cautun M., Deason A. J., Frenk C. S., Grand R. J. J., Marinacci F., 2022, MNRAS, 513, 4107

Carretta E., 2015, ApJ, 810, 148

Carretta E., Bragaglia A., 2023, A&A, 677, A73

Carretta E. et al., 2010, A&A, 520, A95

Carretta E., Lucatello S., Gratton R. G., Bragaglia A., D'Orazi V., 2011, A&A, 533, A69

Carretta E., Gratton R. G., Bragaglia A., D'Orazi V., Lucatello S., 2013a, A&A, 550, A34

Carretta E. et al., 2013b, A&A, 557, A138

Carretta E. et al., 2014, A&A, 564, A60

Chandra V. et al., 2023, preprint (arXiv:2310.13050)

Chen Y., Gnedin O. Y., 2022, MNRAS, 514, 4736

Chen Y., Gnedin O. Y., 2023, MNRAS, 522, 5638

Choksi N., Gnedin O. Y., 2019, MNRAS, 488, 5409

Choksi N., Gnedin O. Y., Li H., 2018, MNRAS, 480, 2343

Clarke A. J. et al., 2019, MNRAS, 484, 3476

Clauwens B., Schaye J., Franx M., Bower R. G., 2018, MNRAS, 478, 3994

Conroy C. et al., 2022, preprint (arXiv:2204.02989)

Côté P., Marzke R. O., West M. J., Minniti D., 2000, ApJ, 533, 869

Côté P., West M. J., Marzke R. O., 2002, ApJ, 567, 853

Crestani J., Alves-Brito A., Bono G., Puls A. A., Alonso-García J., 2019, MNRAS, 487, 5463

Das P., Hawkins K., Jofré P., 2020, MNRAS, 493, 5195

Davison T. A., Norris M. A., Pfeffer J. L., Davies J. J., Crain R. A., 2020, MNRAS, 497, 81

Davoust E., Sharina M. E., Donzelli C. J., 2011, A&A, 528, A70

De Lucia G., Kruijssen J. M. D., Trujillo-Gomez S., Hirschmann M., Xie L., 2023, preprint (arXiv:2307.02530)

Deason A. J., Belokurov V., Sanders J. L., 2019, MNRAS, 490, 3426

Debattista V. P. et al., 2023, ApJ, 946, 118

Dillamore A. M., Belokurov V., Font A. S., McCarthy I. G., 2022, MNRAS, 513, 1867

Dillamore A. M., Belokurov V., Evans N. W., Davies E. Y., 2023, MNRAS, 524, 3596

Dillamore A. M., Belokurov V., Kravtsov A., Font A. S., 2024, MNRAS, 527, 7070

Dinescu D. I., Girard T. M., van Altena W. F., 1999, AJ, 117, 1792

Dornan V., Harris W. E., 2023, ApJ, 950, 179

Eggen O. J., Lynden-Bell D., Sandage A. R., 1962, ApJ, 136, 748

El-Badry K., Quataert E., Weisz D. R., Choksi N., Boylan-Kolchin M., 2019, MNRAS, 482, 4528

Fall S. M., Rees M. J., 1985, ApJ, 298, 18

Forbes D. A., 2020, MNRAS, 493, 847

3212

Forbes D. A., Bridges T., 2010, MNRAS, 404, 1203

Forbes D. A., Read J. I., Gieles M., Collins M. L. M., 2018, MNRAS, 481, 5592

Gaia Collaboration, 2016, A&A, 595, A1

Gaia Collaboration, 2021, A&A, 649, A1

Garver B. R., Nidever D. L., Debattista V. P., Beraldo e Silva L., Khachaturyants T., 2023, ApJ, 953, 128

Gieles M., Gnedin O., 2023, MNRAS, 522, 5340

Gunn J. E., 1980, in Hanes D., Madore B., eds, Globular Clusters. p. 301

Harris W. E., 2010, preprint (arXiv:1012.3224)

Harris W. E., Pudritz R. E., 1994, ApJ, 429, 177

Harris W. E., Blakeslee J. P., Harris G. L. H., 2017, ApJ, 836, 67

Hasselquist S. et al., 2021, ApJ, 923, 172

Hawkins K., Jofré P., Masseron T., Gilmore G., 2015, MNRAS, 453, 758

Helmi A., de Zeeuw P. T., 2000, MNRAS, 319, 657

Helmi A., Babusiaux C., Koppelman H. H., Massari D., Veljanoski J., Brown A. G. A., 2018, Nature, 563, 85

Holtzman J. A. et al., 1996, AJ, 112, 416

Hopkins P. F., 2015, MNRAS, 450, 53

Hopkins P. F. et al., 2018a, MNRAS, 480, 800

Hopkins P. F. et al., 2018b, MNRAS, 480, 800

Horta D. et al., 2020, MNRAS, 493, 3363

Horta D. et al., 2021, MNRAS, 500, 1385

Hudson M. J., Harris G. L., Harris W. E., 2014, ApJ, 787, L5

Hunter J. D., 2007, Comput. Sci. Eng., 9, 90

Johnson C. I., Caldwell N., Rich R. M., Walker M. G., 2017a, AJ, 154, 155 Johnson C. I., Caldwell N., Rich R. M., Mateo M., Bailey John I. I., Clarkson

W. I., Olszewski E. W., Walker M. G., 2017b, ApJ, 836, 168

Johnson C. I., Caldwell N., Rich R. M., Mateo M., Bailey John I. I., Olszewski E. W., Walker M. G., 2017c, ApJ, 842, 24

Johnson C. I., Rich R. M., Caldwell N., Mateo M., Bailey John I. I., Olszewski E. W., Walker M. G., 2018, AJ, 155, 71

Johnson C. I., Caldwell N., Michael Rich R., Mateo M., Bailey J. I., 2019, MNRAS, 485, 4311

Jones E., Oliphant T., Peterson P. et al., 2001, SciPy: Open source scientific tools for Python, http://www.scipy.org/

Kacharov N., Koch A., McWilliam A., 2013, A&A, 554, A81

Keller B. W., Kruijssen J. M. D., Pfeffer J., Reina-Campos M., Bastian N., Trujillo-Gomez S., Hughes M. E., Crain R. A., 2020, MNRAS, 495, 4248

Kobayashi C., Umeda H., Nomoto K., Tominaga N., Ohkubo T., 2006, ApJ, 653, 1145

Kravtsov A. V., Gnedin O. Y., 2005, ApJ, 623, 650

Kravtsov A. V., Vikhlinin A. A., Meshcheryakov A. V., 2018, Astron. Lett., 44, 8

Kruijssen J. M. D., 2015, MNRAS, 454, 1658

Kruijssen J. M. D., Pfeffer J. L., Crain R. A., Bastian N., 2019a, MNRAS, 486, 3134

Kruijssen J. M. D., Pfeffer J. L., Reina-Campos M., Crain R. A., Bastian N., 2019b, MNRAS, 486, 3180

Kruijssen J. M. D. et al., 2020, MNRAS, 498, 2472

Krumholz M. R., McKee C. F., Bland-Hawthorn J., 2019, ARA&A, 57, 227

Lamb M. P., Venn K. A., Shetrone M. D., Sakari C. M., Pritzl B. J., 2015, MNRAS, 448, 42

Lapenna E., Mucciarelli A., Ferraro F. R., Origlia L., Lanzoni B., Massari D., Dalessandro E., 2015, ApJ, 813, 97

Leaman R., VandenBerg D. A., Mendel J. T., 2013, MNRAS, 436, 122

Lee J.-W., Carney B. W., Habgood M. J., 2005, AJ, 129, 251

Li H., Gnedin O. Y., 2014, ApJ, 796, 10

Licquia T. C., Newman J. A., 2015, ApJ, 806, 96

Limberg G., Souza S. O., Pérez-Villegas A., Rossi S., Perottoni H. D., Santucci R. M., 2022, ApJ, 935, 109

Lindegren L. et al., 2021, A&A, 649, A2

Mackereth J. T., Bovy J., 2020, MNRAS, 492, 3631

Malhan K. et al., 2022, ApJ, 926, 107

Marín-Franch A. et al., 2009, ApJ, 694, 1498

Marino A. F. et al., 2015, MNRAS, 450, 815

Marino A. F. et al., 2019, ApJ, 887, 91

Marino A. F. et al., 2021, ApJ, 923, 22

Maschberger T., Kroupa P., 2007, MNRAS, 379, 34

Massari D. et al., 2017, MNRAS, 468, 1249

Massari D., Koppelman H. H., Helmi A., 2019, A&A, 630, L4

McCluskey F., Wetzel A., Loebman S. R., Moreno J., Faucher-Giguere C.-A., 2024, MNRAS, 527, 6926

Minelli A., Mucciarelli A., Massari D., Bellazzini M., Romano D., Ferraro F. R., 2021, ApJ, 918, L32

Montecinos C., Villanova S., Muñoz C., Cortés C. C., 2021, MNRAS, 503, 4336

Monty S. et al., 2023, MNRAS, 522, 4404

Muñoz C. et al., 2018, A&A, 620, A96

Mura-Guzmán A., Villanova S., Muñoz C., Tang B., 2018, MNRAS, 474, 4541

Muratov A. L., Gnedin O. Y., 2010, ApJ, 718, 1266

Murray S. D., Lin D. N. C., 1992, ApJ, 400, 265

Myeong G. C., Evans N. W., Belokurov V., Sanders J. L., Koposov S. E., 2018, ApJ, 863, L28

Myeong G. C., Vasiliev E., Iorio G., Evans N. W., Belokurov V., 2019, MNRAS, 488, 1235

Nadler E. O. et al., 2020, ApJ, 893, 48

Ness M., Asplund M., Casey A. R., 2014, MNRAS, 445, 2994

O'Malley E. M., Chaboyer B., 2018, ApJ, 856, 130

Oliphant T. E., 2015, Guide to NumPy, 2nd edn. CreateSpace Independent Publishing Platform

Origlia L., Valenti E., Rich R. M., 2008, MNRAS, 388, 1419

Pagnini G., Di Matteo P., Khoperskov S., Mastrobuono-Battisti A., Haywood M., Renaud F., Combes F., 2023, A&A, 673, A86

Paust N., Wilson D., van Belle G., 2014, AJ, 148, 19

Pedregosa F. et al., 2011, J. Mach. Learn. Res., 12, 2825

Peebles P. J. E., 1965, ApJ, 142, 1317

Peebles P. J. E., 1984, in Audouze J., Tran Thanh Van J., eds, NATO Advanced Study Institute (ASI) Series C Vol. 117, Formation and Evolution of Galaxies and Large Structures in the Universe. p. 185

Peebles P. J. E., Dicke R. H., 1968, ApJ, 154, 891

Peebles P. J. E., Yu J. T., 1970, ApJ, 162, 815

Pfeffer J., Lardo C., Bastian N., Saracino S., Kamann S., 2021, MNRAS, 500, 2514

Pillepich A. et al., 2018, MNRAS, 475, 648

Qu Y. et al., 2017, MNRAS, 464, 1659

Rain M. J., Villanova S., Munoz C., Valenzuela-Calderon C., 2019, MNRAS, 483, 1674

Recio-Blanco A., 2018, A&A, 620, A194

Reina-Campos M., Kruijssen J. M. D., Pfeffer J. L., Bastian N., Crain R. A., 2019, MNRAS, 486, 5838

Reina-Campos M., Trujillo-Gomez S., Deason A. J., Kruijssen J. M. D., Pfeffer J. L., Crain R. A., Bastian N., Hughes M. E., 2022a, MNRAS, 513, 3025

Reina-Campos M., Keller B. W., Kruijssen J. M. D., Gensior J., Trujillo-Gomez S., Jeffreson S. M. R., Pfeffer J. L., Sills A., 2022b, MNRAS, 517, 3144

Rix H.-W. et al., 2022, ApJ, 941, 45

Schweizer F., 1987, in Faber S. M., ed., Nearly Normal Galaxies. From the Planck Time to the Present. p. 18

Searle L., 1977, in Tinsley B. M., Larson Richard B., Gehret D. C., eds, Evolution of Galaxies and Stellar Populations. p. 219

Searle L., Zinn R., 1978, ApJ, 225, 357

Semenov V. A., Conroy C., Chandra V., Hernquist L., Nelson D., 2023, preprint (arXiv:2306.09398)

Simons R. C. et al., 2017, ApJ, 843, 46

Sneden C., Kraft R. P., Guhathakurta P., Peterson R. C., Fulbright J. P., 2004, AJ, 127, 2162

Souza S. O. et al., 2023, A&A, 671, A45

Spitler L. R., Forbes D. A., 2009, MNRAS, 392, L1

Sun G., Wang Y., Liu C., Long R. J., Chen X., Gao Q., 2023, Res. Astron. Astrophys., 23, 015013

Trujillo-Gomez S., Kruijssen J. M. D., Reina-Campos M., Pfeffer J. L., Keller B. W., Crain R. A., Bastian N., Hughes M. E., 2021, MNRAS, 503, 31

Trujillo-Gomez S., Kruijssen J. M. D., Pfeffer J., Reina-Campos M., Crain R. A., Bastian N., Cabrera-Ziri I., 2023, MNRAS, 526, 5735

Valenti E., Origlia L., Rich R. M., 2011, MNRAS, 414, 2690

Valenzuela L. M., Remus R.-S., McKenzie M., Forbes D. A., 2023, preprint (arXiv:2309.11545)

VandenBerg D. A., Brogaard K., Leaman R., Casagrande L., 2013, ApJ, 775, 134

Vasiliev E., Baumgardt H., 2021, MNRAS, 505, 5978

Vasiliev E., Belokurov V., Evans N. W., 2022, ApJ, 926, 203

Wegg C., Gerhard O., Portail M., 2015, MNRAS, 450, 4050

Wetzel A. et al., 2023, ApJS, 265, 44

Whitmore B. C., Schweizer F., 1995, AJ, 109, 960

Whitmore B. C., Schweizer F., Leitherer C., Borne K., Robert C., 1993, AJ, 106, 1354

Whitmore B. C., Zhang Q., Leitherer C., Fall S. M., Schweizer F., Miller B. W., 1999, AJ, 118, 1551

Yong D., Grundahl F., Nissen P. E., Jensen H. R., Lambert D. L., 2005, A&A, 438, 875

Yong D. et al., 2014, MNRAS, 441, 3396

Zepf S. E., Ashman K. M., English J., Freeman K. C., Sharples R. M., 1999, AJ, 118, 752

Zinn R., 1985, ApJ, 293, 424

Zinn R., 1996, in Morrison H. L., Sarajedini A., eds, ASP Conf. Ser. Vol. 92, Formation of the Galactic Halo...Inside and Out. Astron. Soc. Pac., San Francisco, p. 211

# APPENDIX A: COMPLEMENTING APOGEE GLOBULAR CLUSTER CHEMISTRY WITH LITERATURE VALUES

We have compiled a sample of Galactic GCs with measurements of [Mg/Fe] and [Al/Fe] available both in APOGEE DR17 and in prior spectroscopic studies. This includes NGC 362 (Carretta et al. 2013b), NGC 1851 (Carretta et al. 2011), NGC 2808 (Carretta 2015), NGC 3201 (Marino et al. 2019), NGC 4590 (Lee, Carney & Habgood 2005), NGC 5272 (Sneden et al. 2004), NGC 6121 (Carretta et al. 2013a), NGC 6273 (Johnson et al. 2017b), HP 1 (Barbuy et al. 2016), NGC 6388 (Carretta & Bragaglia 2023), NGC 6553 (Montecinos et al. 2021), NGC 6558 (Barbuy et al. 2018b), NGC 6569 (Johnson et al. 2018), NGC 6715 (Carretta et al. 2010), NGC 6723 (Crestani

et al. 2019), NGC 6752 (Yong et al. 2005), NGC 6809 (Rain et al. 2019), and NGC 7089 (Yong et al. 2014). In the literature, where abundance measurements are available for individual stars we calculate median [Mg/Fe] and [Al/Fe], otherwise we use published mean values.

Fig. A1 compares APOGEE DR17 (*x*-axis) and literature (*y*-axis) median/mean values of [Al/Fe] (first two panels) and [Mg/Fe] (second two panels). Compared to APOGEE DR17, literature values (based on spectroscopic studies mostly in the optical wavelength range) are higher by 0.24 dex for [Al/Fe] and by 0.15 dex for [Mg/Fe]. We subtract these constant offsets (computed as medians of the residuals for each element) from the available literature values to bring them on the same scale with APOGEE DR17.

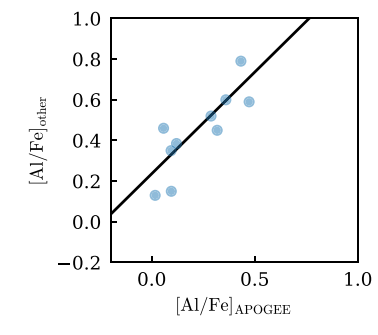
# APPENDIX B: DISTRIBUTION OF ACCRETED TO *IN-SITU* FRACTION IN SIMULATED GALAXIES

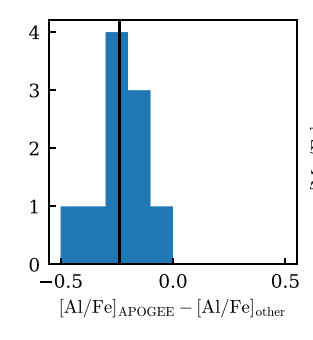
Fig. B1 shows the ratio of accreted stellar mass to *in-situ* stellar mass,  $m_{\rm acc}/m_{in\text{-}situ}$ , in different regions of the total energy-angular momentum space  $E-L_z$  in three MW-sized galaxies (m12c, m12w, m12f) from the FIRE-2 suite. The galaxies m12c and m12w are selected because they are close to the Milky Way in the halo and stellar mass and have the distribution of stars in the  $E-L_z$  similar to the Milky Way. They also have different fractions of accreted stars.

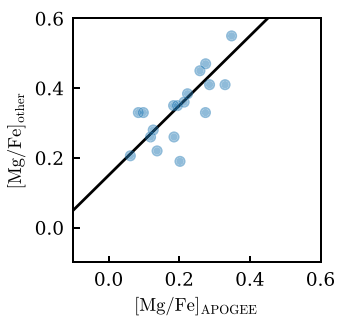
The top row of panels shows results for stellar particles of all metallicities, while the bottom row shows results for stellar particles with [Fe/H] < -1 only. The colour represents the logarithm of  $m_{\rm acc}/m_{in\text{-}situ}$ , as shown on the side colourmap using the divergent colourmap to delineate the transition from the accretion-dominated to the *in-situ* dominated regions better. This boundary is delineated by the white to faint blue colour.

Although the boundary in the top row varies from object to object in detail, reflecting different evolution pathways and merger histories, qualitatively the boundary is similar to that adopted in our classification based on the [Al/Fe] ratio of the MW stars. Specifically, the boundary is quite flat and is at  $E \approx -1.3 \times 10^5 \, \mathrm{km^2/s^2}$  at  $L_z < 2000 \, \mathrm{kpc \, km/s}$  and increases in energy with increasing  $L_z$  at  $L_z > 2000 \, \mathrm{kpc \, km/s}$ .

Comparing bottom and top panels for simulations m12c and m12w shows that the boundary between the accretion and *in-situ* dominated regions in the  $E-L_z$  plane can depend on metallicity. However, we







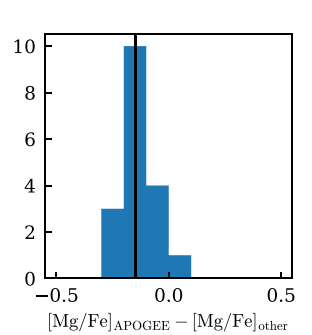


**Figure A1.** Comparison of the chemical abundance values for several MW GCs with measurements both by APOGEE and from other previously published studies. First panel: [Al/Fe] from literature (y-axis) versus [Al/Fe] in APOGEE DR17 (x-axis). Solid line shows 1:1 relation. Second panel: Distribution of differences between [Al/Fe] values based on the APOGEE DR17 and literature. Vertical solid line shows the median offset used to place the literature values on the common scale with APOGEE. Third and Fourth panels: Same as the first two panels but for [Mg/Fe].

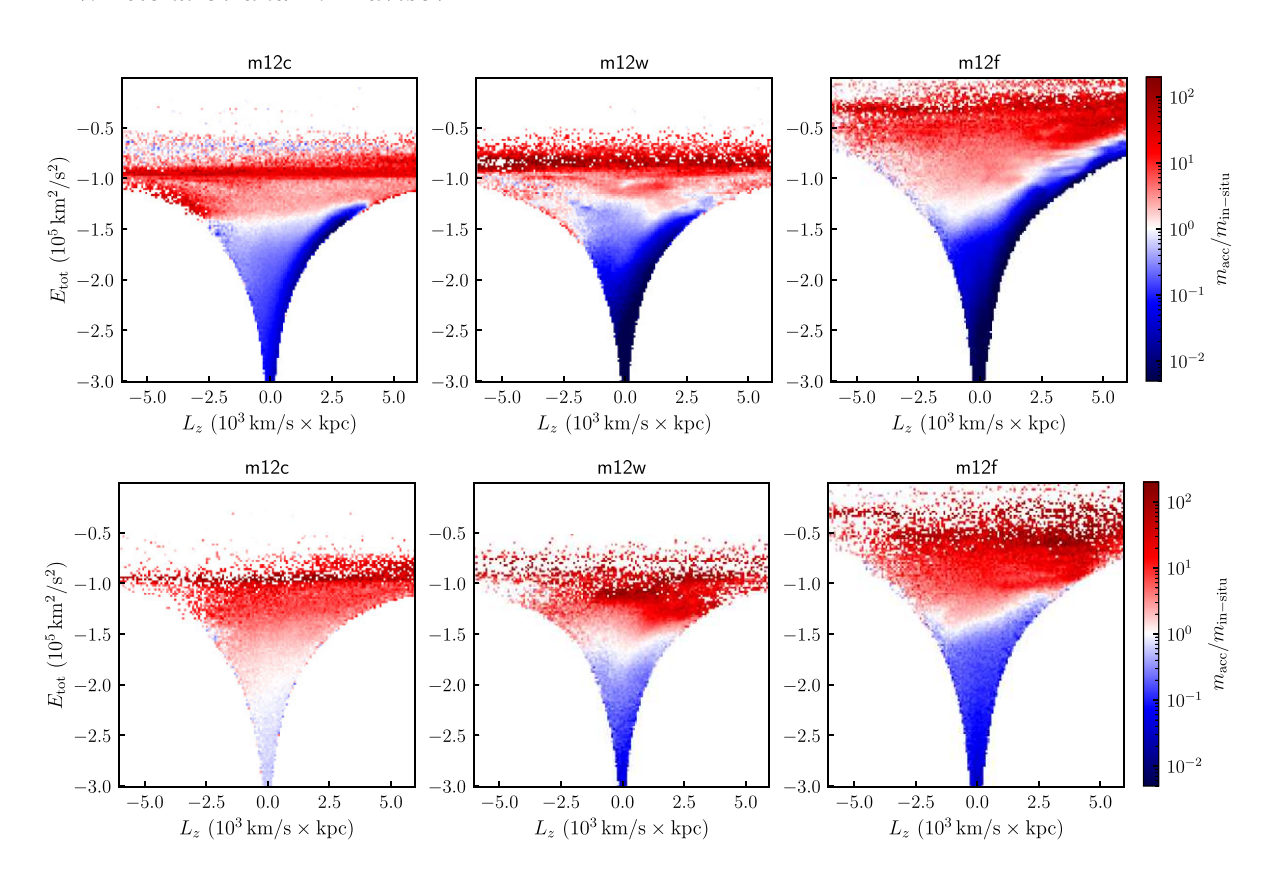


Figure B1. The ratio of accreted stellar mass to in-situ stellar mass,  $m_{acc}/m_{in-situ}$ , in different regions of the total energy-angular momentum space  $E-L_z$  in three MW-sized galaxies (m12c, m12w, m12f) from the FIRE-2 suite. The top row of panels shows results for stellar particles of all metallicities, while the bottom row shows results for stellar particles with [Fe/H] < -1 only. The colour represents the logarithm of  $m_{acc}/m_{in-situ}$ , as shown on the side colourmap using the divergent colourmap to delineate the transition from the accretion-dominated to the in-situ dominated regions better. This boundary is delineated by the white to faint-blue colour.

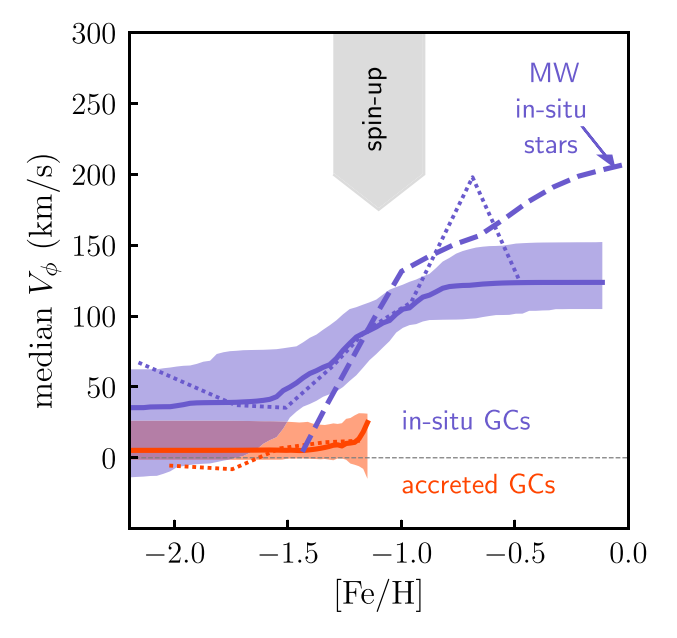


Figure B2. The disc spin-up traced by in-situ globular clusters similar to Fig. 5, but using results of the regression fits of the functional form given by equation (C1) as described in the text of Appendix C. The blue-solid lines shows median of the fits for individual GC bootstrap samples, while blue shaded region shows the region containing 68 per cent of the best fit bootstrap functions at each [Fe/H]. As in Fig. 5, blue dashed lines shows median  $V_{\phi}$  for *in-situ* stars of the Milky Way, as measured in Belokurov & Kravtsov (2022). The red solid line and shaded region show the corresponding results for the accreted GCs. The blue and red dotted lines show medians for the bootstrap samples in the coarse bins shown in Fig. 5.

note that for the MW analysis carried out in Belokurov & Kravtsov (2023) and in this work the boundary is actually calibrated most reliably at the metallicities of  $-1.5 \lesssim [\text{Fe/H}] \lesssim -1$ .

# APPENDIX C: DISC SPIN-UP WITH GLOBULAR CLUSTERS USING FITTING INSTEAD OF BINNING

As an alternative to binning and estimating median and its uncertainty using coarse bins, as was done in Section 4.4, we model the trend of  $V_{\phi}$  with x = [Fe/H] using the sigmoid function that has the shape of a 'soft step':

$$s(x) = \frac{V_{\text{high}}}{\exp(-[10x + x_{\text{sp}}]) + 1} + V_{\text{low}},$$
 (C1)

where  $V_{\rm low}$  and  $V_{\rm high}$  are smallest velocity at metallicities below the spin-up and  $V_{\rm high}$  is the velocity increase from  $V_{\rm low}$  to the maximal velocity at metallicities larger than the spin-up [Fe/H]. The bias parameter  $x_{\rm sp}$  determines the metallicity at which spin-up occurs. The factor of 10 in equation (C1) controls the width of the step and was fixed in the fits to minimize degeneracies between parameters.

Specifically, we carry out the minimal absolute distance regression using metallicities and  $V_{\phi}$  values for individual GCs and find the best-fitting parameters  $V_{\text{low}}$ ,  $V_{\text{high}}$ ,  $x_{\text{sp}}$  minimizing the cost function:

$$C = \sum_{i=1}^{N_{GC}} |s(x) - x_i|.$$
 (C2)

This type of regression approximates the median trend of the data points.

We carry out such regression for 1000 bootstrap resamples of the original GC samples and plot the median and 68 per cent range of the best-fitting functional fits to the bootstrap samples of the *insitu* and accreted samples as solid lines in Fig. B2. Note that we only use accreted clusters with [Fe/H] < -1 in the fit as there are only 3 accreted clusters in our classification at higher metallicities, which makes the fit unconstrained at these higher metallicities. The figure compares results obtained by this method with the medians obtained using bootstrap samples in coarse bins shown in Fig. 5 and shows that both methods produce similar results. We conclude therefore that detection of spin-up at  $[Fe/H] \approx -1.3 \div -1$  in *in-situ* GCs is robust.

### APPENDIX D: LIST OF GC CLASSIFICATIONS

Table D1 presents the list of globular clusters used in this study and their classification using our method (1 is *in-situ*, 0 is accreted). The last column provides comments for individual clusters that may be misclassified by this method, where NSC stands for the Nuclear Star Cluster based on the analysis of Pfeffer et al. (2021) and where we used analysis of element abundance ratios presented in Section 5.1 to indicate the *in-situ* (accreted) clusters with the ratios similar to those of accreted (*in-situ*) systems.

**Table D1.** The names of the globular clusters used in this study and their classification using our method (1 is *in-situ*, 0 is accreted).

Cluster name 2MASS-GC01	In-situ/accreted (1/0) 1	Comments
2MASS-GC02	1	
AM 1	0	
AM 4	0	
Arp 2	0	
BH 140	1	
BH 261	1	
Crater	0	
Djorg 1	1	
Djorg 2	1	
E 3	1	
ESO 280-SC06	0	
ESO 452-SC11 Eridanus	1	
FSR 1716	0 1	
FSR 1710 FSR 1735	1	
FSR 1758	0	
Gran 1	1	
Gran 2	1	
Gran 3	1	
Gran 5	1	
HP 1	1	
IC 1257	0	
IC 1276	1	
IC 4499	0	
Laevens 3	0	
Liller 1	1	
Lynga 7	1	
NGC 104	1	
NGC 1261	0	
NGC 1851	0	
NGC 1904	0	
NGC 2298	0	
NGC 2419	0	
NGC 2808	0	
NGC 288	0	[Al/Fe] and [Mg/Fe]
		consistent with in-situ, see
1100 2201	•	Fig. 11
NGC 3201	0	
NGC 362	0	
NGC 4147	0	
NGC 4372	1	
NGC 4590	0	
NGC 4833 NGC 5024	1 0	
NGC 5024 NGC 5053	0	
NGC 5033	1	likely NSC/accreted
NGC 5272	0	inkery 145C/accreted
NGC 5272 NGC 5286	0	[Al/Fe] and [Mg/Fe]
1100 3200	v	consistent with <i>in-situ</i> , see
		Fig. 11
NGC 5466	0	8
NGC 5634	0	
NGC 5694	0	
NGC 5824	0	
NGC 5897	1	
NGC 5904	0	
NGC 5927	1	[Al/Fe] and [Mg/Fe]
		consistent with being
		accreted, see Fig. 11
NGC 5946	1	
NGC 5986	1	
NGC 6093	1	
NGC 6101	0	
NGC 6121	1	

Table D1 - continued

NGC 6139 NGC 6144 NGC 6171 NGC 6205 NGC 6218 NGC 6218 NGC 6229 NGC 6229 NGC 6235 NGC 6254 NGC 6254 NGC 6256 NGC 6256 NGC 6273 NGC 6273 NGC 6273 NGC 6284 NGC 6287 NGC 6287 NGC 6293 NGC 6304 NGC 6316 NGC 6316 NGC 6325 NGC 6325 NGC 6325 NGC 6333 NGC 6341 NGC 6341 NGC 6341 NGC 6355 NGC 6355 NGC 6355 NGC 6356 NGC 6388 NGC 6388 NGC 6388 NGC 6388 NGC 6388 NGC 6397 NGC 6401 NGC 6401 NGC 6402 NGC 6401 NGC 6406 NGC 6440 NGC 6455 NGC 6558 NGC 6558 NGC 6558 NGC 6558 NGC 6558 NGC 6558 NGC 6569 NGC 6564 NGC 6566 NGC 6569 NGC 6568 NGC 6568 NGC 6568 NGC 6667 NGC 66687 NGC 66682 NGC 66681 NGC 66681 NGC 66682 NGC 66682 NGC 66682 NGC 66682 NGC 66681 NGC 66682 NGC 66681 NGC 66682			
NGC 6171 NGC 6205 NGC 6218 NGC 6218 NGC 6229 NGC 6235 NGC 6235 NGC 6254 NGC 6254 NGC 6256 NGC 6256 NGC 6256 NGC 6257 NGC 6273 NGC 6284 NGC 6287 NGC 6287 NGC 6304 NGC 6304 NGC 6316 NGC 6316 NGC 6316 NGC 6325 NGC 6333 NGC 6341 NGC 6355 NGC 6355 NGC 6355 NGC 6355 NGC 6366 NGC 6388 NGC 6388 NGC 6397 NGC 6397 NGC 6397 NGC 6401 NGC 6401 NGC 6426 NGC 6440 NGC 6440 NGC 6453 NGC 6559 NGC 6559 NGC 6559 NGC 6559 NGC 6559 NGC 6559 NGC 6558 NGC 6558 NGC 6569 NGC 6558 NGC 6558 NGC 6558 NGC 6558 NGC 6569 NGC 6584 NGC 6566 NGC 6569 NGC 6584 NGC 6566 NGC 6569 NGC 6566 NGC 6566 NGC 6569 NGC 6584 NGC 6566 NGC 6569 NGC 6584 NGC 6566 NGC 6584 NGC 65667 NGC 6667 NGC 66667 NGC 6667 NGC 66688 NGC 6667 NGC 66688 NGC 66688 NGC 66688 NGC 66688 NGC 66687 NGC 66681 NGC 66681 NGC 66681 NGC 66683 NGC 66683 NGC 66683 NGC 66683 NGC 66683 NGC 66684 NGC 66683 NGC 66684 NGC 66684 NGC 66683 NGC 66684 NGC 66688 NGC 66682	NGC 6139	1	
NGC 6205	NGC 6144	1	
NGC 6218 NGC 6229 NGC 6235 NGC 6235 NGC 6235 NGC 6254 NGC 6254 NGC 6256 NGC 6266 NGC 6266 NGC 6273 NGC 6284 NGC 6287 NGC 6287 NGC 6287 NGC 6304 NGC 6304 NGC 6316 NGC 6316 NGC 6325 NGC 6333 NGC 6341 NGC 6341 NGC 6355 NGC 6355 NGC 6355 NGC 6356 NGC 6366 NGC 6366 NGC 6366 NGC 6368 NGC 6360 NGC 637 NGC 6397 NGC 6388 NGC 6397 NGC 6401 NGC 6401 NGC 641 NGC 6426 NGC 6426 NGC 6453 NGC 6537 NGC 6538 NGC 6538 NGC 6539 NGC 6539 NGC 6539 NGC 6539 NGC 6530 NGC 6530 NGC 6530 NGC 6530 NGC 6531 NGC 6531 NGC 6531 NGC 6531 NGC 6531 NGC 6533 NGC 6544 NGC 6553 NGC 6553 NGC 6553 NGC 6554 NGC 6553 NGC 6558 NGC 6569 NGC 6564 NGC 6656 NGC 6664 NGC 6667 NGC 66667 NGC 66667 NGC 66668 NGC 66681 NGC 66682 NGC 66682 NGC 66681 NGC 66681 NGC 66681 NGC 66681 NGC 66681 NGC 66682 NGC 66682 NGC 66682 NGC 66682 NGC 66681 NGC 66682 NGC 66681 NGC 66682 NGC 66684 NGC 6688	NGC 6171	1	
NGC 6229  NGC 6235  NGC 6254  NGC 6254  NGC 6256  NGC 6266  NGC 6266  NGC 6267  NGC 6273  NGC 6284  NGC 6287  NGC 6287  NGC 6283  NGC 6304  NGC 6304  NGC 6316  NGC 6316  NGC 6333  NGC 6333  NGC 6341  NGC 6352  NGC 6355  NGC 6355  NGC 6355  NGC 6356  NGC 6366  NGC 6388  NGC 6388  NGC 6388  NGC 6402  NGC 641  NGC 6426  NGC 6426  NGC 6537  NGC 6539  NGC 6544  NGC 6553  NGC 6553  NGC 6569  NGC 6584  NGC 66666  NGC 66666  NGC 66667  NGC 66666  NGC 66667  NGC 66668  NGC 66681  NGC 6683  NGC 66681  NGC 66682  NGC 66681  NGC 66681  NGC 66681  NGC 66682  NGC 66681  NGC 66681  NGC 66682	NGC 6205	1	
NGC 6229  NGC 6235  NGC 6254  NGC 6254  NGC 6256  NGC 6266  NGC 6266  NGC 6267  NGC 6273  NGC 6284  NGC 6287  NGC 6287  NGC 6283  NGC 6304  NGC 6304  NGC 6316  NGC 6316  NGC 6333  NGC 6333  NGC 6341  NGC 6352  NGC 6355  NGC 6355  NGC 6355  NGC 6356  NGC 6366  NGC 6388  NGC 6388  NGC 6388  NGC 6402  NGC 641  NGC 6426  NGC 6426  NGC 6537  NGC 6539  NGC 6544  NGC 6553  NGC 6553  NGC 6569  NGC 6584  NGC 66666  NGC 66666  NGC 66667  NGC 66666  NGC 66667  NGC 66668  NGC 66681  NGC 6683  NGC 66681  NGC 66682  NGC 66681  NGC 66681  NGC 66681  NGC 66682  NGC 66681  NGC 66681  NGC 66682		1	
NGC 6235			
NGC 6254 NGC 6256 NGC 6256 NGC 6266 NGC 6266 NGC 6273 NGC 6284 NGC 6287 NGC 6287 NGC 6293 NGC 6304 NGC 6316 NGC 6316 NGC 6325 NGC 6325 NGC 6341 NGC 6341 NGC 6355 NGC 6355 NGC 6355 NGC 6356 NGC 6366 NGC 6368 NGC 6388 NGC 6388 NGC 6401 NGC 6401 NGC 6401 NGC 6401 NGC 6401 NGC 6440 NGC 6440 NGC 6440 NGC 6453 NGC 6553 NGC 6528 NGC 6528 NGC 6528 NGC 6528 NGC 6528 NGC 6535 NGC 6535 NGC 6536 NGC 6536 NGC 6536 NGC 6537 NGC 6553 NGC 6564 NGC 6568 NGC 6569 NGC 6558 NGC 65684 NGC 65684 NGC 65684 NGC 66642 NGC 66642 NGC 66642 NGC 66641 NGC 66581 NGC 65684 NGC 6588 NGC 6588 NGC 6569 NGC 65684 NGC 65684 NGC 65684 NGC 66645 NGC 66646 NGC 66646 NGC 66646 NGC 66646 NGC 66647 NGC 66648 NGC 66648 NGC 66648 NGC 66687 NGC 66688			
NGC 6256			
NGC 6266			
NGC 6273			
NGC 6284   1   NGC 6287   1   NGC 6293   1   NGC 6304   1   NGC 6304   1   NGC 6316   1   NGC 6325   1   NGC 6333   1   NGC 6333   1   NGC 6341   0   NGC 6352   1   NGC 6352   1   NGC 6355   1   [Al/Fe] and [Mg/Fe] consistent with being accreted, see Fig. 11   NGC 6356   1   NGC 6366   1   NGC 6388   1   [Al/Fe] and [Mg/Fe] consistent with being accreted, see Fig. 11   NGC 6397   1   NGC 6401   1   NGC 6402   1   NGC 6426   0   NGC 6440   1   NGC 6440   1   NGC 6453   1   NGC 6553   1   NGC 6552   1   NGC 6552   1   NGC 6553   1   NGC 6553   1   NGC 6559   1   NGC 6559   1   NGC 6559   1   NGC 6551   NGC 6554   1   NGC 6555   1   NGC 6555   1   NGC 6555   1   NGC 6556   1   NGC 6556   1   NGC 6556   1   NGC 6557   NGC 6569   1   NGC 6560   1   NGC 6560   1   NGC 6558   1   NGC 6560   1   NGC 6560   1   NGC 6560   1   NGC 6560   1   NGC 6660   1   NG			Litraly, NCC/a agreeted
NGC 6287			likely NSC/accreted
NGC 6293			
NGC 6304 NGC 6316 NGC 6325 NGC 6333 NGC 6333 NGC 6341 NGC 6352 NGC 6352 NGC 6355 NGC 6355 NGC 6355 NGC 6356 NGC 6366 NGC 6366 NGC 6368 NGC 6388 NGC 6397 NGC 6401 NGC 6402 NGC 6402 NGC 6426 NGC 6453 NGC 6453 NGC 6558 NGC 6558 NGC 6558 NGC 6558 NGC 6558 NGC 6558 NGC 6569 NGC 6564 NGC 6564 NGC 6564 NGC 6566 NGC 6564 NGC 6566 NGC 66642 NGC 66668 NGC 6668			
NGC 6316 NGC 6325 NGC 6333 NGC 6341 NGC 6342 NGC 6352 NGC 6355 NGC 6355 NGC 6355 NGC 6366 NGC 6366 NGC 6360 NGC 6380 NGC 6380 NGC 6380 NGC 6397 NGC 6401 NGC 6402 NGC 6404 NGC 6453 NGC 6440 NGC 6453 NGC 6540 NGC 6522 NGC 6522 NGC 6528 NGC 6539 NGC 6539 NGC 6539 NGC 6540 NGC 6544 NGC 6553 NGC 6540 NGC 6540 NGC 6553 NGC 6569 NGC 6564 NGC 6566 NGC 6666 NGC 6667 NGC 6667 NGC 6667 NGC 6668 NGC 6668 NGC 6638 NGC 6638 NGC 6638 NGC 6638 NGC 6638 NGC 6638 NGC 6642 NGC 6644 NGC 6553 NGC 6569 NGC 6569 NGC 66661 NGC 6667 NGC 6668			
NGC 6325			
NGC 6333			
NGC 6341 NGC 6342 NGC 6352 NGC 6355 NGC 6355 NGC 6355 NGC 6355 NGC 6356 NGC 6366 NGC 6366 NGC 6380 NGC 6388 NGC 6388 NGC 6397 NGC 6401 NGC 6401 NGC 6402 NGC 6426 NGC 6441 NGC 6453 NGC 6553 NGC 6552 NGC 6558 NGC 6558 NGC 6553 NGC 6558 NGC 6558 NGC 6558 NGC 6584 NGC 6584 NGC 6624 NGC 6624 NGC 6624 NGC 6626 NGC 6626 NGC 6627 NGC 6626 NGC 6626 NGC 6638 NGC 6642 NGC 6642 NGC 6642 NGC 6644 NGC 6658 NGC 6668	NGC 6325		
NGC 6342 NGC 6352 NGC 6355 NGC 6355 NGC 6355 NGC 6366 NGC 6366 NGC 6388 NGC 6388 NGC 6397 NGC 6401 NGC 6402 NGC 6426 NGC 6440 NGC 6453 NGC 6558 NGC 6558 NGC 6558 NGC 6522 NGC 6535 NGC 6535 NGC 6535 NGC 6535 NGC 6540 NGC 6544 NGC 6553 NGC 6558 NGC 6558 NGC 6558 NGC 6569 NGC 6584 NGC 6624 NGC 6624 NGC 6626 NGC 6624 NGC 6626 NGC 6626 NGC 6637 NGC 6638 NGC 6638 NGC 6638 NGC 6642 NGC 6638 NGC 6642 NGC 6638 NGC 6644 NGC 6559 NGC 6569 NGC 6569 NGC 6569 NGC 6584 NGC 6584 NGC 6658 NGC 6662 NGC 6637 NGC 6638 NGC 6642	NGC 6333	1	
NGC 6352 NGC 6355 NGC 6355 NGC 6355 NGC 6355 NGC 6366 NGC 6362 NGC 6366 NGC 6388 NGC 6388 NGC 6388 NGC 6397 NGC 6401 NGC 6402 NGC 6404 NGC 6440 NGC 6440 NGC 6453 NGC 6544 NGC 6552 NGC 6528 NGC 6528 NGC 6535 NGC 6535 NGC 6536 NGC 6540 NGC 6540 NGC 6541 NGC 6544 NGC 6553 NGC 6558 NGC 6558 NGC 6569 NGC 6584 NGC 6686 NGC 6686 NGC 6687 NGC 6688	NGC 6341	0	
NGC 6355  1	NGC 6342	1	
consistent with being accreted, see Fig. 11  NGC 6366  NGC 6366  NGC 6380  NGC 6388  I [Al/Fe] and [Mg/Fe] consistent with being accreted, see Fig. 11  NGC 6397  NGC 6401  NGC 6426  NGC 6426  NGC 6440  NGC 6440  NGC 6453  NGC 6553  NGC 6552  NGC 6522  NGC 6558  I [Al/Fe] and [Mg/Fe] consistent with being accreted, see Fig. 11  NGC 6555  NGC 6540  NGC 6541  NGC 6541  NGC 6553  NGC 6558  NGC 6558  NGC 6569  NGC 6569  NGC 6564  NGC 6564  NGC 6564  NGC 6566  NGC 66667  NGC 6668	NGC 6352	1	
consistent with being accreted, see Fig. 11  NGC 6356	NGC 6355	1	[Al/Fe] and [Mg/Fe]
accreted, see Fig. 11  NGC 6356  NGC 6362  NGC 6366  NGC 6380  NGC 6388  1  NGC 6388  1  NGC 6397  NGC 6401  NGC 6402  NGC 6426  NGC 6440  NGC 6440  NGC 6453  NGC 6537  NGC 6517  NGC 6522  NGC 6528  1  NGC 6528  1  NGC 6539  NGC 6539  NGC 6540  NGC 6544  NGC 6540  NGC 6544  NGC 6553  NGC 6558  NGC 6558  NGC 6558  NGC 6569  NGC 6584  NGC 6664  NGC 6664  NGC 6666  NGC 6668			
NGC 6356 NGC 6362 NGC 6366 NGC 6380 NGC 6388 NGC 6388 NGC 6388 NGC 6397 NGC 6401 NGC 6402 NGC 6402 NGC 6440 NGC 6440 NGC 6441 NGC 6453 NGC 6453 NGC 6557 NGC 6522 NGC 6528 NGC 6528 NGC 6539 NGC 6539 NGC 6540 NGC 6541 NGC 6544 NGC 6553 NGC 6558 NGC 6558 NGC 6558 NGC 6569 NGC 6584 NGC 6585 NGC 6586 NGC 6586 NGC 6586 NGC 6586 NGC 6587 NGC 6588 NGC 6688 NGC 6668 NGC 6637 NGC 6638 NGC 6638 NGC 6638 NGC 6638 NGC 6638 NGC 6642			
NGC 6362 NGC 6366 NGC 6380 NGC 6388  1 NGC 6388 1 NGC 6388 1 NGC 6397 NGC 6401 NGC 6402 NGC 6426 NGC 6440 NGC 6441 NGC 6453 NGC 6453 NGC 6552 NGC 6522 NGC 6522 NGC 6528 1 NGC 6535 NGC 6539 NGC 6540 NGC 6541 NGC 6541 NGC 6544 NGC 6553 NGC 6564 NGC 6558 NGC 6569 NGC 6568 NGC 6564 NGC 6568 NGC 6564 NGC 6564 NGC 6564 NGC 6564 NGC 6566 NGC 6666 NGC 6667 NGC 6668	NGC 6356	1	decreted, see Fig. 11
NGC 6366 1 NGC 6380 1 NGC 6388 1 [Al/Fe] and [Mg/Fe] consistent with being accreted, see Fig. 11 NGC 6397 1 NGC 6401 1 NGC 6402 1 NGC 6402 1 NGC 6426 0 NGC 6440 1 NGC 6453 1 NGC 6453 1 NGC 6553 1 NGC 6522 1 NGC 6528 1 [Al/Fe] and [Mg/Fe] consistent with being accreted, see Fig. 11  NGC 6535 1 NGC 6535 1 NGC 6539 1 NGC 6540 1 NGC 6541 1 NGC 6553 1 NGC 6558 1 NGC 6558 1 NGC 6569 1 NGC 6564 1 NGC 6565 1 NGC 6566 1 NGC 6666 1 NGC 6626 1 NGC 6626 1 NGC 6637 1 NGC 6638 1 NGC 6638 1 NGC 6642 1			
NGC 6380 1 NGC 6388 1 [Al/Fe] and [Mg/Fe] consistent with being accreted, see Fig. 11 NGC 6397 1 NGC 6401 1 NGC 6402 1 NGC 6426 0 NGC 6440 1 NGC 6440 1 NGC 6453 1 NGC 6553 1 NGC 6522 1 NGC 6528 1 [Al/Fe] and [Mg/Fe] consistent with being accreted, see Fig. 11 NGC 6535 1 NGC 6539 1 NGC 6540 1 NGC 6541 1 NGC 6553 1 NGC 6558 1 NGC 6558 1 NGC 6569 1 NGC 6564 1 NGC 6564 1 NGC 6564 1 NGC 6565 1 NGC 6566 1 NGC 6666 1 NGC 6667 1 NGC 6668 1 NGC 6637 1 NGC 6638 1 NGC 6642			
NGC 6388  1			
Consistent with being accreted, see Fig. 11  NGC 6397  NGC 6401  NGC 6402  NGC 6426  NGC 6440  NGC 6440  NGC 6441  NGC 6453  NGC 6496  NGC 6517  NGC 6522  NGC 6528  1  IAl/Fe] and [Mg/Fe] consistent with being accreted, see Fig. 11  NGC 6535  NGC 6539  NGC 6540  NGC 6541  NGC 6553  NGC 6554  NGC 6558  NGC 6558  NGC 6569  NGC 6569  NGC 6584  NGC 6560  NGC 6626  NGC 6627  NGC 6637  NGC 6638  NGC 6638  NGC 6638  NGC 6640			[A1/Ea] and [Ma/Ea]
NGC 6397 NGC 6401 NGC 6402 NGC 6426 NGC 6426 NGC 6440 NGC 6441 NGC 6453 NGC 6496 NGC 6517 NGC 6522 NGC 6522 NGC 6528  NGC 6528  NGC 6535 NGC 6539 NGC 6539 NGC 6540 NGC 6541 NGC 6553 NGC 6554 NGC 6558 NGC 6558 NGC 6569 NGC 6569 NGC 6584 NGC 6585 NGC 6586 NGC 6666 NGC 6677 NGC 6637 NGC 6638 NGC 6638 NGC 6638 NGC 6638 NGC 6642	NGC 0388	1	consistent with being
NGC 6401 1 NGC 6402 1 NGC 6402 1 NGC 6426 0 NGC 6440 1 NGC 6441 1 NGC 6453 1 NGC 6496 1 NGC 6517 1 NGC 6522 1 NGC 6528 1 [Al/Fe] and [Mg/Fe] consistent with being accreted, see Fig. 11 NGC 6535 1 NGC 6539 1 NGC 6540 1 NGC 6541 1 NGC 6553 1 NGC 6558 1 NGC 6558 1 NGC 6558 1 NGC 6569 1 NGC 6560 1 NGC 6584 0 [Al/Fe] and [Mg/Fe] consistent with in-situ, see Fig. 11 NGC 6626 1 NGC 6627 1 NGC 6638 1 NGC 6638 1 NGC 6638 1 NGC 6638 1 NGC 6642	NGC 6397	1	decreted, see Fig. 11
NGC 6402			
NGC 6426 NGC 6440 NGC 6441 NGC 6441 NGC 6453 NGC 6496 NGC 6517 NGC 6522 NGC 6522 NGC 6528  1 NGC 6528  1 NGC 6535 NGC 6539 NGC 6540 NGC 6541 NGC 6553 NGC 6558 NGC 6558 NGC 6558 NGC 6569 NGC 6569 NGC 6584 NGC 6584 NGC 6584 NGC 6669 NGC 6664 NGC 6667 NGC 6637 NGC 6638 NGC 6638 NGC 6638 NGC 6642 NGC 6642 NGC 6642 NGC 6642 NGC 6642 NGC 6668			
NGC 6440  NGC 6441  NGC 6453  NGC 6496  NGC 6517  NGC 6522  NGC 6528  NGC 6528  NGC 6535  NGC 6539  NGC 6540  NGC 6541  NGC 6553  NGC 6553  NGC 6558  NGC 6558  NGC 6569  NGC 6569  NGC 6584  NGC 6688  NGC 6637  NGC 6638  NGC 6638  NGC 6638  NGC 6642			
NGC 6441 1 1 NGC 6453 1 1 NGC 6496 1 1 NGC 6517 1 1 NGC 6522 1 1 NGC 6528 1 [Al/Fe] and [Mg/Fe] consistent with being accreted, see Fig. 11 NGC 6535 1 1 NGC 6539 1 1 NGC 6540 1 1 NGC 6541 1 1 NGC 6544 1 1 NGC 6553 1 1 NGC 6553 1 1 NGC 6558 1 1 NGC 6558 1 1 NGC 6558 1 1 NGC 6569 1 1 NGC 6584 0 [Al/Fe] and [Mg/Fe] consistent with in-situ, see Fig. 11 NGC 6624 1 1 NGC 6626 1 1 NGC 6637 1 1 NGC 6638 1 1 NGC 6638 1 1 NGC 6642 1 1			
NGC 6453 NGC 6496 NGC 6517 NGC 6517 NGC 6522 NGC 6528  1 NGC 6528 1 NGC 6528 1 NGC 6535 NGC 6539 NGC 6540 NGC 6541 NGC 6544 NGC 6553 NGC 6553 NGC 6553 NGC 6558 NGC 6558 NGC 6569 NGC 6569 NGC 6584 0 IAl/Fe] and [Mg/Fe] consistent with in-situ, see Fig. 11 NGC 6624 NGC 6637 NGC 6638 NGC 6638 NGC 6642 1 NGC 6642			
NGC 6496  NGC 6517  NGC 6522  NGC 6528  1  I [Al/Fe] and [Mg/Fe] consistent with being accreted, see Fig. 11  NGC 6535  NGC 6539  NGC 6540  NGC 6541  NGC 6544  NGC 6553  NGC 6553  NGC 6558  NGC 6558  NGC 6569  NGC 6584  O [Al/Fe] and [Mg/Fe] consistent with in-situ, see Fig. 11  NGC 6624  NGC 6626  NGC 6637  NGC 6638  NGC 6642			
NGC 6517 NGC 6522 NGC 6528  1 NGC 6528  1 NGC 6528  1 NGC 6528  1 NGC 6535 NGC 6539 NGC 6540 NGC 6541 NGC 6541 NGC 6553 NGC 6553 NGC 6553 NGC 6558 NGC 6558 NGC 6559 NGC 6569 NGC 6584  0  1 NGC 6626 NGC 6637 NGC 6638 NGC 6632 NGC 6642			
NGC 6522 1 NGC 6528 1 [Al/Fe] and [Mg/Fe] consistent with being accreted, see Fig. 11  NGC 6535 1 NGC 6539 1 NGC 6540 1 NGC 6541 1 NGC 6544 1 NGC 6553 1 NGC 6553 1 NGC 6558 1 NGC 6558 1 NGC 6569 1 NGC 6584 0 [Al/Fe] and [Mg/Fe] consistent with in-situ, see Fig. 11  NGC 6624 1 NGC 6626 1 NGC 6637 1 NGC 6638 1 NGC 6642 1			
NGC 6528  1			
consistent with being accreted, see Fig. 11  NGC 6535  NGC 6539  NGC 6540  NGC 6541  NGC 6544  NGC 6553  NGC 6553  NGC 6558  NGC 6558  NGC 6569  NGC 6584  O  [Al/Fe] and [Mg/Fe] consistent with in-situ, see Fig. 11  NGC 6624  NGC 6626  NGC 6637  NGC 6638  NGC 6642  1			
NGC 6539 1 NGC 6540 1 NGC 6541 1 NGC 6544 1 NGC 6553 1 NGC 6558 1 NGC 6569 1 NGC 6584 0 [Al/Fe] and [Mg/Fe] consistent with in-situ, see Fig. 11 NGC 6624 1 NGC 6626 1 NGC 6637 1 NGC 6638 1 NGC 6642 1	NGC 6528	1	consistent with being
NGC 6539 1 NGC 6540 1 NGC 6541 1 NGC 6544 1 NGC 6553 1 NGC 6558 1 NGC 6569 1 NGC 6584 0 [Al/Fe] and [Mg/Fe] consistent with in-situ, see Fig. 11 NGC 6624 1 NGC 6626 1 NGC 6637 1 NGC 6638 1 NGC 6642 1	NGC 6535	1	-
NGC 6540 1 NGC 6541 1 NGC 6544 1 NGC 6553 1 NGC 6558 1 NGC 6569 1 NGC 6584 0 [Al/Fe] and [Mg/Fe] consistent with in-situ, see Fig. 11 NGC 6624 1 NGC 6626 1 NGC 6637 1 NGC 6638 1 NGC 6642 1			
NGC 6541 1 1			
NGC 6544 1 NGC 6553 1 NGC 6558 1 NGC 6569 1 NGC 6584 0 [Al/Fe] and [Mg/Fe] consistent with in-situ, see Fig. 11 NGC 6624 1 NGC 6626 1 NGC 6637 1 NGC 6638 1 NGC 6642 1			
NGC 6553 1 NGC 6558 1 NGC 6569 1 NGC 6584 0 [Al/Fe] and [Mg/Fe] consistent with in-situ, see Fig. 11 NGC 6624 1 NGC 6626 1 NGC 6637 1 NGC 6638 1 NGC 6642 1			
NGC 6558 1 NGC 6569 1 NGC 6584 0 [Al/Fe] and [Mg/Fe] consistent with in-situ, see Fig. 11 NGC 6624 1 NGC 6626 1 NGC 6637 1 NGC 6638 1 NGC 6642 1			
NGC 6569 1 NGC 6584 0 [Al/Fe] and [Mg/Fe] consistent with <i>in-situ</i> , see Fig. 11 NGC 6624 1 NGC 6626 1 NGC 6637 1 NGC 6638 1 NGC 6642 1			
NGC 6584 0 [Al/Fe] and [Mg/Fe] consistent with <i>in-situ</i> , see Fig. 11  NGC 6624 1  NGC 6626 1  NGC 6637 1  NGC 6638 1  NGC 6642 1			
consistent with <i>in-situ</i> , see Fig. 11  NGC 6624  NGC 6626  1  NGC 6637  NGC 6638  1  NGC 6642  1			[A1/E-1 15A /E-3
NGC 6624 1 NGC 6626 1 NGC 6637 1 NGC 6638 1 NGC 6642 1	NGC 6584	0	consistent with in-situ, see
NGC 6626 1 NGC 6637 1 NGC 6638 1 NGC 6642 1	NCC 6624	1	rig. 11
NGC 6637 1 NGC 6638 1 NGC 6642 1			
NGC 6638 1 NGC 6642 1			
NGC 6642 1			
NGC 6652 1			
	NGC 6652	1	

**Table D1.** (continued). The names of the globular clusters used in this study and their classification using our method (1 is *in-situ*, 0 is accreted). The last column provides comments for individual clusters that may be misclassified by this method. NSC = Nuclear Star Cluster based on the analysis of Pfeffer et al. (2021).

Cluster name	In-situ/accreted (1/0)	Comments
NGC 6656	1	Comments
NGC 6681	1	
NGC 6712	1	
NGC 6715	0	
NGC 6717	1	
NGC 6723	1	
NGC 6749	1	
NGC 6752	1	
NGC 6760	1	
NGC 6779	0	
NGC 6809	1	
NGC 6838	1	
NGC 6864	0	
NGC 6934	0	
NGC 6981	0	
NGC 7006	0	GI 1 1FF /FF 1
NGC 7078	1	Shows enhanced [Eu/Fe]
		and may be accreted (see
		Monty et al. in preparation)
NGC 7089	0	
NGC 7099	1	
NGC 7492	0	
Pal 1	1	
Pal 10	1	
Pal 11	1	
Pal 12	0	
Pal 13	0	
Pal 14	0	
Pal 15	0	
Pal 2	0	
Pal 3	0	
Pal 4	0	
Pal 5	0	
Pal 6	1	
Pal 8	1	
Patchick 126	1	
Pyxis	0	
Rup 106	0	
Sagittarius II	0	
Terzan 1	1	
Terzan 10	1	
Terzan 12	1	
Terzan 2	1	
Terzan 3	1	
Terzan 4	1	
Terzan 5	1	
Terzan 6	1	
Terzan 7	0	
Terzan 8	0	
Terzan 9	1	
Ton 2	1	
UKS 1	1	
VVV-CL001	1	
VVV-CL160	0	
Whiting 1	0	

This paper has been typeset from a TEX/IATEX file prepared by the author.